Published in final edited form as:

Nat Immunol. 2022 January ; 23(1): 75–85. doi:10.1038/s41590-021-01093-y.

Congenital iRHOM2 deficiency causes ADAM17 dysfunction and environmentally directed immunodysregulatory disease

Satoshi Kubo[1], **Jill M. Fritz**[1,18], **Hayley M. Raquer-McKay**[1,19], **Rhea Kataria**[1], **Ivan Vujkovic-Cvijin**[2,20], **Ahmad Al-Shaibi**[3], **Yikun Yao**[1], **Lixin Zheng**[1], **Juan Zou**[1], **Alex D. Waldman**[1], **Xinyi Jing**[1], **Taylor K. Farley**[2,4], **Ann Y. Park**[1], **Andrew J. Oler**[5], **Adrian K. Charles**[6], **Melanie Makhlouf**[3], **Eman H. AbouMoussa**[3], **Reem Hasnah**[3], **Luis R. Saraiva**[3,7,8], **Sundar Ganesan**[9], **Abdulrahman Ahmed Al-Subaiey**[8], **Helen Matthews**[1], **Emilio Flano**[10], **Hyun Hee Lee**[10], **Alexandra F. Freeman**[11], **Asena Pınar Sefer**[12,13,14], **Ersin Sayar**[15], **Erkan Çakır**[16], **Elif Karakoc-Aydiner**[12,13,14], **Safa Baris**[12,13,14], **Yasmine Belkaid**[2,17], **Ahmet Ozen**[12,13,14,21,✉], **Bernice Lo**[3,8,21,✉], **Michael J. Lenardo**[1,21,✉]

[1]Molecular Development of the Immune System Section, Laboratory of Immune System Biology and Clinical Genomics Program, Division of Intramural Research, National Institute of Allergy and Infectious Diseases, National Institutes of Health, Bethesda, MD, USA.

[2]Metaorganism Immunity Section, Laboratory of Host Immunity and Microbiome, National Institute of Allergy and Infectious Diseases, National Institutes of Health, Bethesda, MD, USA.

[3]Research Branch, Sidra Medicine, Doha, Qatar.

[4]Kennedy Institute of Rheumatology, Nuffield Department of Orthopaedics, Rheumatology and Musculoskeletal Sciences, University of Oxford, Oxford, UK.

[5]Bioinformatics and Computational Biosciences Branch, Office of Cyber Infrastructure and Computational Biology, National Institute of Allergy and Infectious Diseases, National Institutes of Health, Bethesda, MD, USA.

[6]Department of Anatomical Pathology, Sidra Medicine, Doha, Qatar.

[7]Monell Chemical Senses Center, Philadelphia, PA, USA.

[8]College of Health and Life Sciences, Hamad Bin Khalifa University, Doha, Qatar.

✉**Correspondence and requests for materials** should be addressed to Ahmet Ozen, Bernice Lo or Michael J. Lenardo. ahmet.ozen@marmara.edu.tr; blo@sidra.org; lenardo@nih.gov.

Author contributions

S.K., J.M.F., H.M.R.-M. and R.K. performed experiments and contributed to the study design, overall review and writing of the manuscript. I.V.-C., A.A.-S., Y.Y., L.Z., J.Z., A.D.W., X.J., T.K.F., A.Y.P., A.J.O., A.K.C., M.M., E.H.A.M., R.H., L.R.S., S.G., A.A.A.-S., E.F., H.H.L., A.F.F. and Y.B. performed experiments and analyzed and interpreted data. H.M., A.P.S., E.S., E.C., E.K.-A., S.B. and A.O. managed and oversaw care of the patients. A.O. and B.L. participated in the study design and coordination. M.J.L. contributed to the study design, overall review and writing of the manuscript and coordinated the overall direction of the study. All authors have read and approved the final manuscript.

Competing interests

H.H.L. and E.F. were employees of Merck Sharp & Dohme Corp., a subsidiary of Merck & Co., Inc., Kenilworth, NJ, USA. All other authors have no competing interests.

Extended data is available for this paper at https://doi.org/10.1038/s41590-021-01093-y.

Supplementary information The online version contains supplementary material available at https://doi.org/10.1038/s41590-021-01093-y.

[9]Biological Imaging Section, Research Technologies Branch, National Institute of Allergy and Infectious Diseases, National Institutes of Health, Bethesda, MD, USA.

[10]Discovery Oncology and Immunology, Merck & Co., Inc., Boston, MA, USA.

[11]Laboratory of Clinical Immunology and Microbiology, National Institute of Allergy and Infectious Diseases, National Institutes of Health, Bethesda, MD, USA.

[12]Division of Allergy and Immunology, Marmara University School of Medicine, Istanbul, Turkey.

[13]Istanbul Jeffrey Modell Diagnostic Center for Primary Immunodeficiency Diseases, Istanbul, Turkey.

[14]The Isil Berat Barlan Center for Translational Medicine, Istanbul, Turkey.

[15]Department of Pediatric Gastroenterology, Altinbas University Medical Park Bahcelievler Hospital, Istanbul, Turkey.

[16]Division of Pediatric Pulmonology, Department of Pediatrics, Bezmialem Vakif University, School of Medicine, Istanbul, Turkey.

[17]National Institute of Allergy and Infectious Diseases Microbiome Program, National Institutes of Health, Bethesda, MD, USA.

[18]Present address: Cooley, LLP in Washington, Washington, DC, USA.

[19]Present address: Immunology Program, Stanford University School of Medicine, Stanford, CA, USA.

[20]Present address: F. Widjaja Foundation Inflammatory Bowel and Immunobiology Research Institute and Department of Biomedical Sciences, Cedars-Sinai Medical Center, Los Angeles, CA, USA.

[21]These authors jointly supervised this work: Ahmet Ozen, Bernice Lo, Michael J. Lenardo.

Abstract

We report a pleiotropic disease due to loss-of-function mutations in RHBDF2, the gene encoding iRHOM2, in two kindreds with recurrent infections in different organs. One patient had recurrent pneumonia but no colon involvement, another had recurrent infectious hemorrhagic colitis but no lung involvement and the other two experienced recurrent respiratory infections. Loss of iRHOM2, a rhomboid superfamily member that regulates the ADAM17 metalloproteinase, caused defective ADAM17-dependent cleavage and release of cytokines, including tumor-necrosis factor and amphiregulin. To understand the diverse clinical phenotypes, we challenged *Rhbdf2*$^{-/-}$ mice with *Pseudomonas aeruginosa* by nasal gavage and observed more severe pneumonia, whereas infection with *Citrobacter rodentium* caused worse inflammatory colitis than in wild-type mice. The fecal microbiota in the colitis patient had characteristic oral species that can predispose to colitis. Thus, a human immunodeficiency arising from iRHOM2 deficiency causes divergent disease phenotypes that can involve the local microbial environment.

Both genes and environment define healthy and diseased phenotypes. Many identifiable environmental factors, including geography, chemicals, infections and others, influence

phenotypes associated with specific genetic variants. A classic example is phenylalanine hydroxylase deficiency[1]. Dietary intake of phenylalanine causes phenylketonuria with growth and neurological effects whereas a phenylalanine-free diet averts the neurodevelopmental phenotype but causes metabolic abnormalities1. Different exposures can account for the variable phenotypic expression. For the immune system, a key environmental factor is the mucosal microbiome. Conceptually, a gene defect could exhibit different organ pathology depending on the microbiome at different anatomical sites, but how this occurs in primary immunodeficiencies is unclear.

iRHOMs are rhomboid-like pseudoenzymes that facilitate trafficking, stabilization and cell surface processing of key regulatory proteins. iRHOMs contain a cytosolic N-terminal domain and an iRHOM homology domain that promote client protein interactions. One chief client of iRHOM2 is ADAM17 (tumor-necrosis factor-α (TNF-α) converting enzyme, or TACE), a metalloproteinase that processes signaling molecules, including TNF and TNF receptors[2,3]. Dysregulation of these factors can cause autoimmunity, immunodeficiency and cancer, and iRHOMs have evolved to tightly control ADAM17 function[4]. iRHOMs bind immature pro-ADAM17 in the endoplasmic reticulum and then chaperone the molecule to the Golgi apparatus for cleavage by furin convertases to generate enzymatically active, mature ADAM17 (refs.[5,6]). At the cell surface, ADAM17 stays bound to iRHOMs to prevent endocytosis and lysosomal degradation. Upon stimulation, ERK-dependent phosphorylation of the iRHOM2 N-terminal cytoplasmic tail recruits 14-3-3 proteins, releasing ADAM17 to proteolytically process nearby substrates including membrane-bound TNF[7,8]. Additional substrates of ADAM17 include epidermal growth factor (EGF) family members, such as amphiregulin (AREG), which promotes epithelial cell growth and differentiation, development and regeneration after infections[9,10]. How a human genetic deficiency of iRHOM2 alters cytokine production and wound healing is unknown.

Two iRHOM proteins, iRHOM1 and iRHOM2, are encoded in metazoans by the RHBDF1 and RHBDF2 genes, respectively. iRHOM1 is expressed in most tissues, but not immune cells, and *Rhbdf1* deficiency impairs postnatal development and survival[11–13]. By contrast, iRHOM2 is largely immune cell restricted and *Rhbdf2*$^{-/-}$ mice are viable with no pathological abnormalities[6,13,14]. Nevertheless, *Rhbdf2*$^{-/-}$ mice infected with *Listeria monocytogenes* have increased bacterial burden and reduced survival as a result of diminished TNF release[6]. However, they exhibit reduced disease in lupus models as well as renal and lung injuries due to lowered inflammation and oxidative stress[15–17]. iRHOM2 also controls the type I interferon viral response proteins ‘mitochondrial antiviral-signaling’ (MAVS) and ‘stimulator of interferon genes’ (STING), respectively[18,19]. Human dominant-activating mutations in *RHBDF2* develop tylosis, or hyperkeratosis of the hands, feet and esophagus, conferring a high risk for esophageal cancer[20,21]. Keratinocytes from patients with tylosis secrete increased EGFR ligands including AREG, heparin-binding EGF-like growth factor (HB-EGF) and transforming growth factor-α (TGF-α) (refs.[22–24]). This striking human phenotype due to activating mutations in *RHBDF2* raises the question of what phenotypes would accompany germline deficiency.

Results

Immunodeficiency patients with homozygous mutation of RHBDF2.

We studied two unrelated kindreds comprising four patients with recurrent infections targeting different organs (Fig. 1a–c and Table 1). In kindred 1, patient 1 (P1) was a 7-yr-old male born to healthy consanguineous parents in rural Turkey with fever and wheezing at 3 months of age (Fig. 1b). He experienced multiple hospitalizations for severe respiratory infections treated with antibiotics and immunoglobulin infusions (Fig. 1b). Chest computed tomography from one hospitalization showed bilateral pneumonia (Fig. 1c) and two large pneumatoceles (Fig. 1b). The patient also experienced eczema, recurrent otitis media, mild hepatosplenomegaly, a skin abscess and high serum IgE. However, naïve and memory B and T cells and natural killer (NK) cells were normal (Table 1). In kindred 2, P4 was born to consanguineous parents and underwent multiple hospitalizations for diarrhea and abdominal upset with sepsis. An endoscopy of P4 showed hemorrhagic colitis and mucosal changes (Fig. 1c and Extended Data Fig. 1a). P2 and P3 had recurrent upper respiratory infections but are otherwise healthy (Fig. 1a–c, Extended Data Fig. 1a and Table 1). These patients are Syrian refugees and personal hygiene may be hindered by their poor economic condition.

Whole exome sequencing identified frameshift premature termination variants in the *RHBDF2* gene encoding iRHOM2. In kindred 1, c.1887_1888delCT, p.Cys630LeufsTer19 caused a stop codon in the iRHOM homology domain at amino acid 648 (Fig. 1a,d and Table 1). We prioritized this variant because it was homozygous, absent from gnomAD and other databases and no other variants segregated with disease. The mother declined genetic testing, but the father and brother were heterozygous for this variant and clinically unaffected (Fig. 1a). In kindred 2, the homozygous variant c.2170_2171delCA, p.Gln724ValfsTer105 was found in P2, P3 and P4; both parents and two siblings were heterozygous and two other siblings were mutation-free (Fig. 1a,d and Table 1). Although the eczema, recurrent infections, pneumatoceles and high serum IgE in P1 overlap with STAT3-deficient hyper IgE syndrome (HIES), the patient lacked mucocutaneous candidiasis, skeletal or connective tissue abnormalities, or its characteristic facial appearance[25]. P1's HIES score (which distinguishes particular gene deficiencies causing a HIES-like phenotype with a cut-off value of 40) was 27, and no mutations were found in *STAT3*, *DOCK8*, *PGM3*, *SPINK5*, *TYK2* and *IL6ST*, or genes associated with colitis[26,27].

The GTEx database shows that iRHOM2 messenger RNA is high in the spleen and peripheral blood cells (Extended Data Fig. 1b). Analyzing human single-cell RNA-sequencing (scRNA-seq) data revealed that iRHOM2 is high in lymphocytes, monocytes and NK cells, while iRHOM1 is not expressed in immune cells (Fig. 1e and Extended Data Fig. 1c). We found that the iRHOM2 protein was absent in T cells from all patients, whereas the heterozygous parents had intermediate levels of iRHOM2 protein (Fig. 1f). These results indicated that our patients' mutations cause recessive loss-of-function (LOF) alleles.

Impaired TNF secretion in patients' T cells.

iRHOMs control the proteolytic processing and stabilization of ADAM17 in its catalytically active form[5–8]. Comparing patients' whole T cell lysates with those from healthy

controls (HCs), we observed ADAM17 was predominantly in its pro-, or immature, high-molecular-weight form rather than its mature, lower-molecular-weight form, reflecting failed iRHOM2-guided trafficking (Fig. 2a). Moreover, the wild-type sibling had normal levels of cleavage while the heterozygous parents had intermediate cleavage, showing that ADAM17 processing corresponds stoichiometrically to iRHOM2 expression (compare Fig. 2a with Fig. 1f). *ADAM17* mRNA levels were equivalent in all subjects' T cells (Extended Data Fig. 2a).

TNF, a pro-inflammatory cytokine, mediates innate and adaptive immunity[28]. TNF is synthesized as a membrane-bound protein (membrane TNF (mTNF), 26 kDa) that is cleaved by ADAM17 on the cell surface to release soluble TNF (17 kDa)[29,30]. We observed that T cells from all patients had excess surface mTNF (Fig. 2b,c and Extended Data Fig. 2b). The heterozygous parents both exhibited intermediate increases in mTNF which, together with the intermediate level of iRHOM2 protein and ADAM17 cleavage, supports a gene dosage effect (Fig. 2b). Accordingly, soluble TNF was significantly lower in supernatants from T cell receptor (TCR)-stimulated patient T cells in vitro compared with HCs including unaffected siblings (Fig. 2d). Additionally, patient monocytes stimulated with lipopolysaccharide (LPS) had excess mTNF (Extended Data Fig. 2c). The increased mTNF phenotype was recapitulated with both single-guide RNA (sgRNA)–CRISPR-mediated knockout and short interfering RNA (siRNA)-mediated knockdown of *RHBDF2* in HC T cells (Fig. 2e,g and Extended Data Fig. 2d,e). Furthermore, knocking out ADAM17 in HC T cells produced this same phenotype, showing that iRHOM2 deficiency increases mTNF by inhibiting ADAM17 maturation (Fig. 2f,g and Extended Data Fig. 2f). Both patient and knockout cells showed increased mean fluorescence intensity, indicating greater mTNF per cell (Extended Data Fig. 2g,h). Overexpression of iRHOM2 in patient T cells by retroviral transduction of the wild-type *RHBDF2* coding sequence reversed the increased mTNF expression, linking the patients' RHBHF gene defect with the mTNF abnormality (Fig. 2h,i and Extended Data Fig. 2i). Agreeing with these in vitro results, TNF was detected at significantly lower levels in serum from patients compared with HCs or unaffected siblings (Fig. 2k). Thus, iRHOM2 deficiency impaired TNF release both in vitro and in vivo in all patients.

Interestingly, iRHOM2 overexpression suppressed mTNF in HC T cells, demonstrating that iRHOM2 is rate-limiting for regulating mTNF (Extended Data Fig. 2j). We therefore hypothesized that RHBDF2 expression is controlled by T cell activation. Indeed, we found that stimulating T cells with TCR agonists increased RHBDF2 but not RHBDF1 mRNA (Fig. 2j). Moreover, we found that phorbol myristate acetate (PMA) stimulation of dendritic cells and macrophages, but not neutrophils or eosinophils, induced higher mTNF in *Rhbdf2*$^{-/-}$ mice expression than in wild-type mice (Extended Data Figs. 2k and 6). Thus, iRHOM2 mRNA is rate-limiting and inducible during adaptive as well as innate immune responses to facilitate cytokine maturation and release.

As one of our iRHOM2-deficient patients resembled STAT3 deficiency, we examined mTNF in HIES patient cells with *STAT3* LOF mutations. We found that T cells from STAT3 LOF patients did not show an increase in mTNF after stimulation (Extended Data Fig. 2l).

Hence, the phenotypic similarities between LOF STAT3 and iRHOM2 deficiency are likely mTNF-independent.

Apart from TNF, ADAM17 also cleaves over 80 substrates[31], many of which are involved in immune signaling and regulation. For example, CD62L (l-selectin), a cell adhesion molecule processed by ADAM17 that is normally reduced by anti-CD3 stimulation, remained high in patient T cells (Fig. 2l). Taken together, we could conclude the patient's T cells and monocytes cannot secrete important immune molecules such as TNF by a failure of ADAM17 maturation.

Multi-omics analyses of patients reveal key immune defects.

To further understand the infections and cytokine alterations observed in the patients, we conducted broad multi-omics analyses of patient specimens (Fig. 3 and Extended Data Fig. 3). First, we studied patient serum with a Luminex multiplex system that detects 48 cytokine, chemokine and growth factor analytes. We found 16 cytokines and chemokines were reliably detectable in the patient and HC serum (Extended Data Fig. 3a). Compared with HCs, none were increased, but IL-8 and TNF, which are ADAM17-dependent, and eotaxin-1 (CCL11) were significantly decreased in the patient samples (Fig. 3a)[32]. We also noted a trend, though not statistically significant, that certain other cytokines not processed by ADAM17, including IL-1β, MCP-1 and IL-1Rα, were lower in the patients (Fig. 3a).

We next carried out transcriptomic analyses on patient whole blood. Our analysis showed increased immunoglobulin gene transcription, consistent with abnormally high mTNF in vivo and its known ability to costimulate B cells for immunoglobulin synthesis (Extended Data Fig. 3b)[33]. We also noted that LEPREL2, a prolyl 3-hydroxylase 3, is strikingly reduced indicating that proline hydroxylation, characteristic of proteins involved in tissue integrity, could be defective[34]. Most importantly, gene set enrichment analysis (GSEA) revealed reduced transcription of genes involved in leukocyte migration, defense response to other organisms and neutrophil-mediated immunity (Fig. 3b and Extended Data Fig. 3c). Diminished expression of these gene sets likely contributes to the poor control of infections in our patients. We observed no significant differences in TNF, IL-8, eotaxin and IL-1β mRNA expression, and other known substrates of ADAM17. This finding indicates that an iRHOM2 deficiency regulates these cytokines post-transcriptionally, likely via post-translational processing (Extended Data Fig. 3d,e).

Next, we investigated dynamic transcriptomic changes in patients' T cells. We stimulated HC and patient samples with PMA for 3, 6, 12 and 21 h and performed RNA sequencing (RNA-seq). While PMA stimulation caused a large overall increase in mRNAs in HC T cells, we observed almost equivalent increased and decreased mRNAs in patient T cells (Extended Data Fig. 3f). We first cataloged gene sets with increased transcription (Extended Data Fig. 3g). We found that for HC cells at 3 h, there was a strong induction of cytokine production and TNF response genes (Extended Data Fig. 3g). Additionally, genes for acute inflammatory response and cytokine secretion were highly induced at 6 h, and those for cell chemotaxis were induced at 12 h. The gene sets for 'response to molecule of bacterial origin' and regeneration were enriched at 21 h (Extended Data Fig. 3g). Compared with HCs, the GSEA revealed less induction at 3 h of the genes for

cytokine production and response to TNF in the patient samples (Fig. 3d). Thus, iRHOM2 deficiency alters the normal transcriptional program of T cells starting early after activation and continues to affect subsequent cellular responses. Moreover, the lack of TNF secretion caused by iRHOM2 deficiency reduces the gene sets responding to TNF and, at 3 h, overall lymphocyte activation was diminished in the patients compared with HCs (Fig. 3e). The GSEA of 'response to molecule of bacterial origin' was decreased at later time points (Fig. 3d).

Since normal cytokine expression depends on vesicle and membrane architecture and function, we performed comprehensive lipidomics using trapped ion mobility separation times of flight mass spectrometry (TimsTOF-LCMS, Bruker). Principal component analysis (PCA) revealed distinct clusters of patient and HC replicate samples, indicating these two groups have notably different lipid profiles (Fig. 3f). Most strikingly, the majority of phosphatidylcholine lipid species (PtdCho) were decreased in the patients' T cells (Fig. 3g). PtdCho species are the most abundant phospholipids in mammalian cell membranes and reductions can cause defective cytokine release, especially for the cleavage and secretion of TNF[35]. Hence, we found secondary lipid abnormalities that can exacerbate the cytokine abnormalities and immunodeficiency.

iRHOM2 deficiency results in susceptibility to pneumonia.

Previous studies show that iRHOM2 knockout, *Rhbdf2*$^{-/-}$, mice do not develop spontaneous disease under laboratory conditions. We therefore asked whether iRHOM2 deficiency increases susceptibility to specific environmental triggers of inflammatory/infectious disease. We tested the response of *Rhbdf2*$^{-/-}$ mice to pneumonia caused by *Pseudomonas aeruginosa* which mimics a type of bacterial lung infection occurring in immunodeficient patients and requires TNF for bacterial clearance[36]. We inoculated the mice with 5×10^8 colony-forming units (c.f.u.) of *P. aeruginosa* via nasal gavage and measured body weight. Over 3 d, the body weight dropped in all mice, with a statistically greater decrease in *Rhbdf2*$^{-/-}$ mice compared with wild-type mice (Fig. 4a). The *Rhbdf2*$^{-/-}$ mice also had worse survival (Fig. 4b). On day 3, we examined the lungs and found that there was an average of 1×10^5 greater *P. aeruginosa* c.f.u., implying defective bacterial clearance in the *Rhbdf2*$^{-/-}$ mice (Fig. 4c). Moreover, the gross anatomy of the lung showed abnormal condensed hyperemic tissue and microscopy showed severe pathological changes including hemorrhage and alveolar wall destruction (Fig. 4d). We also observed lower serum TNF levels in the infected *Rhbdf2*$^{-/-}$ mice despite greater infection and lung damage, conditions that normally cause high TNF levels (Fig. 4e). Thus, the *Rhbdf2*$^{-/-}$ mice are incapable of releasing TNF normally and manage the *P. aeruginosa* infection poorly.

Given that P1 harbors large pneumatoceles, we hypothesized that lung epithelium repair might be defective due to reduced growth factor secretion. We purified epithelial cells by removing CD45$^+$ hematopoietic cells and stromal cells from disaggregated lung tissue taken from *Rhbd2f*$^{-/-}$ mice and found defective ADAM17 maturation (Fig. 4f and Extended Data Fig. 4a). We also studied the human lung cancer A549, H1299 and PC9 cell lines which are models for type II pneumocytes. We found in each line that an iRHOM1 knockout alone had slightly lowered levels of mature ADAM17, but a knockout of iRHOM2 or both

iRHOM1/2 severely reduced ADAM17 maturation (Fig. 4g and Extended Data Fig. 4b). We further confirmed that the knockout/knockdown efficiency for iRHOM1 or iRHOM2 was comparable and specific (Extended Data Fig. 4c–f). Patient lung epithelial cells were unavailable, but these data indicate iRHOM2 dominantly governs ADAM17 processing in mammalian lung epithelial cell lines. AREG, an ADAM17-activated growth factor, promotes mitogenesis and differentiation of epithelial cells[37]. We observed decreased AREG secretion in parallel to reduced mature ADAM17 in A549 cells (Fig. 4h and Extended Data Fig. 4b). TGF-α was undetectable.

In vitro scratch assays have been developed as a model for cell migration and proliferation during tissue repair and regeneration[38]. We found that an iRHOM2 knockout in A549 and H1299 cells reduced scratch closure (Fig. 4i,j and Extended Data Fig. 4i). Adding a combination of ADAM17-dependent growth factors, AREG, TGF-α and HB-EGF, greatly improved scratch closure (Fig. 4i,j and Extended Data Fig. 4j). Moreover, iRHOM2 knockout in PC9 cells, which have mutations in the EGFR gene resulting in constitutively activated signaling, did not affect scratch closure (Extended Data Fig. 4k). These combined findings substantiate our conjecture that an iRHOM2 deficiency impairs cell migration and proliferation due to the loss of EGFR-related growth factor secretion.

iRHOM2 deficiency causes more severe infectious colitis.

To further investigate P4's recurrent colitis, we examined the microbiome in P2, P3 and P4 and found that P4 had a strikingly different microbial composition from his siblings and unrelated HCs (Extended Data Fig. 5a). Importantly, P4's gut microbiota displayed species similarities with the oral microbiome (Fig. 5a and Extended Data Fig. 5b). Ectopic oral microbiota are enriched in the gut of subjects with gastrointestinal inflammatory disorders, are associated with human ulcerative colitis and exacerbate inflammation in murine models of colitis[39,40]. To further understand the impact of gut microbes, we investigated the susceptibility of *Rhbdf2*$^{-/-}$ mice to bacterial-mediated colitis. We chose to study noninvasive bacterial infection in the mouse gastrointestinal tract using *Citrobacter rodentium*, a mouse pathogen controlled by T helper 17 cells (T_H17) responses, whose pathogenesis resembles enteropathogenic and enterohaemorrhagic *Escherichia coli*[41–44]. We infected *Rhbdf2*$^{-/-}$ mice with *C. rodentium* and measured c.f.u. in the stool. In wild-type mice, the bacterial colonization increased steadily over 9 d before falling by 15 d (Fig. 5b). In *Rhbdf2*$^{-/-}$ mice, the c.f.u. rose at day 3, and remained higher than wild-type mice for 13 d (Fig. 5b). Histopathological analyses revealed that despite normal colonic crypt length, the *Rhbdf2*$^{-/-}$ mice had significant goblet cell loss (Fig. 5c and Extended Data Fig. 5c,d). Similar to our patients, CD4 and CD8 T cells from the lamina propria in *Rhbdf2*$^{-/-}$ mice had elevated mTNF during colitis, and lower total serum TNF levels (Fig. 5d–f). Moreover, the IL-6 receptor (IL-6R)—which complexes with IL-6 and the membrane protein gp130 to activate STAT3—remained membrane-tethered during colitis in *Rhbdf2*$^{-/-}$ mice (Fig. 5g). IL-6 and subsequent STAT3 signaling are critical signals for the differentiation and maintenance of T_H17 cells, which secrete IL-17 and IL-22 to restrain *C. rodentium* infection[41,45–47]. We found reduced IL-17A and IL-17F in colonic CD8 cells and IL-17F in colonic CD4 cells of *Rhbdf2*$^{-/-}$ mice, with modest decreases of IL-22 in CD8 cells but no change in IFN-γ (Fig. 5h and Extended Data Fig. 6). These decreases occurred despite the increased *C. rodentium*

burden which would be expected to increase host T_H17 cells. Thus, iRHOM2 potentially influences T_H17 cell function through the IL-6/gp130/STAT3 pathway.

We also examined in vitro wound healing using the human colorectal adenocarcinoma SW620 cell line following CRISPR deletion of iRHOMs (Extended Data Fig. 5e). Depletion of iRHOM1 had little effect, but depletion of iRHOM2 reduced ADAM17 maturation (Fig. 5i). However, in vitro scratch assays showed the iRHOM2 knockout did not reduce wound healing (Fig. 5j,k). These results differed from A549 and H1299 lung cells which required iRHOM2 for scratch closure.

Collectively, the pathogen challenges that we carried out in iRHOM2-deficient mice validate the mechanism by which human patients develop disease.

Discussion

We describe a human primary immunodeficiency caused by mutations in the RHBDF2 gene leading to loss of iRHOM2. The complete lack of iRHOM2 protein expression led to different clinical phenotypes, prompting us to investigate environmental causes. We found that known human pathogens, *P. aeruginosa* and *C. rodentium*, exacerbated disease in *Rhbdf2*$^{-/-}$ mice, resembling the divergent patient phenotypes. The pathogens in our patients are not identified, but our data illustrate that iRHOM2 modulates immunity against respiratory and bowel infections. Moreover, P4 manifested ectopic oral microbiota in the gut, likely promoting inflammation and colitis[39,40]. Interestingly, despite the soluble TNF defect, we have not observed mycobacterial infections. Possibly increased mTNF in the patient T cells confers protection against mycobacterial infection[48].

The iRHOM2/ADAM17 axis affects over 80 substrates[31]. We broadly classify ADAM17 substrates by function: immune system, development/differentiation and others. Immune protective substrate deficiencies include TNF, lymphotoxin-α, TNF receptor (TNF-R) and IL-6R. Furthermore, ADAM17 substrates with cell adhesion functions (CD62L and CD44) could impact our patients by adversely affecting leukocyte migration. Major development/differentiation substrates include EGFR family members, which stimulate epithelial cell proliferation. We expect these defects contribute to P1's scarring and slow healing. It is also known that iRHOM2 controls MAVS and STING proteins, so defects in these molecules could account for the susceptibility of P2 and P3 to recurrent upper respiratory infections. Nevertheless, given the crucial role of TNF in defense against bacterial infections, the failure of its release from the cell surface likely majorly contributes towards the disease phenotype of severe recurrent bacterial infections[49,50].

iRHOM2 is expressed across the majority of human immune cell subsets, but iRHOM1 is expressed minimally, if at all, in immune cells. Our in vitro and ex vivo data from patients show that iRHOM2 is necessary and sufficient for ADAM17 maturation in immune cells. On the other hand, the closely related iRHOM1 may support ADAM17 maturation in iRHOM2-deficient cells outside of the immune compartment[14]. Thus, different tissues may have unique requirements for iRHOM2 in wound healing. Since TNF drives rheumatoid arthritis and other inflammatory diseases, iRHOM2 is an attractive therapeutic target.

Our investigation shows heterozygous humans have roughly half the wild-type levels of iRHOM2 and processed ADAM17. We also observed that iRHOM2 overexpression reduced mTNF in HC T cells, indicating that iRHOM2 is rate-limiting for cleaved end-product, which is consistent with the gene dosage effect in heterozygotes and the fact that iRHOM2 complexes with ADAM17 to ensure its stability at the cell surface[5,6,8]. We discovered that T cell activation induces iRHOM2 expression, perhaps to upregulate this pathway during adaptive immune responses. This facet of iRHOM2 regulation might help guide the development of new therapeutics.

Our multi-omics data revealed in vivo consequences of iRHOM2 deficiency in humans. Little is known about dynamic lipidomic changes in primary immunodeficiencies. Our lipidomics mass spectrometry revealed patients' T cells had a marked deficiency of PtdCho. Previous work shows PtdCho is crucial for the secretion of cytokines such as TNF[35]. Future work will investigate how decreased PtdCho levels are caused by an iRHOM2 deficiency. Dynamic biological processes using time-series gene expression data following PMA stimulation revealed the patient T cells to have major decreases in the gene sets for cytokine production and response to TNF. This result indicates that the impaired TNF secretion impacts patients' T cells by affecting not only TNF soluble levels, but also additional genes responsible for responding to infections. Therefore, we could confirm the lack of TNF secretion has a key role in shaping this disease.

In summary, we characterize an inborn error of immunity that we term 'iRHOM deficiency with Respiratory and Intestinal inflammation and cytokine Secretion defect' (IRIS), illustrating the biological mechanisms of iRHOM2 in preventing recurrent infections at different mucosal locations. One patient had recurrent pneumonia but no colon involvement, and another had recurrent colitis but no lung involvement, although they have the same in vitro phenotypic expression related to immunodeficiency. Different phenotypes of IRIS patients depend on the microbial 'environment', emphasizing that often overlooked external factors determine what physicians see in the clinic. Our study provides insights into the biochemical regulation of iRHOM2 in human immunity and its potential therapeutic applications.

Online content

Any methods, additional references, Nature Research reporting summaries, source data, extended data, supplementary information, acknowledgements, peer review information; details of author contributions and competing interests; and statements of data and code availability are available at https://doi.org/10.1038/s41590-021-01093-y.

Methods

Study designs.

All studies were conducted with a sample size of 3–15 per group (in vitro and in vivo). These numbers were chosen based on hundreds of experiments. For animal experiments, investigators were blinded during analysis using ear tag number codes that were broken after

data were acquired and quantified. For other experiments, investigators were not blinded to genotypes to prevent any mislabeling of different groups.

Human subjects.

All enrolled subjects provided written, informed consent and data were collected through protocols following local ethics and institutional review board (IRB) recommendations. The P1 kindred was enrolled on National Institutes of Health (NIH) Protocol 06-I-0015 (clinicaltrials.gov NCT00246857). IRB approval was obtained from the NIH IRB 02/16/2021. The P2 kindred consented to a protocol approved by the Sidra Medicine Institutional Review Board, no. 1500768, approved 24 May 2021.

Mice.

Animal studies were performed under protocols LISB 19E and LISB 10E, which were approved by the National Institute of Allergy and Infectious Diseases (NIAID) Animal Care and Use Committee. To generate *Rhbdf2*$^{-/-}$ mice, C57BL6/N Rhbdf2$^{tm1b(KOMP)Wtsi}$ sperm containing the tm1b reporter-tagged deletion allele (post-Cre) was obtained from the Knockout Mouse Project Repository (Mutant Mouse Regional Resource Center, UC Davis). In vitro fertilization was performed using Rhbdf2$^{tm1b(KOMP)Wtsi}$ sperm and eggs isolated from superovulated wild-type C57BL6/N females and subsequently transferred into pseudopregnant recipient females. Heterozygous mice bred our wild-type and *Rhbdf*$^{-/-}$ mice.

In vitro culture of cell lines.

293T cells (CRL-3216), A549 cells (CCL-185), H1299 cells (CRL-5803), H1975 cells (CRL-5908) and SW620 cells (CCL-227) were purchased from ATCC. PC9 cells were purchased from Sigma Aldrich (9007180). A549 cells were cultured in complete F-12K medium (10% FBS, 2 mM glutamine, 100 μg ml^{-1} penicillin and 100 μg ml^{-1} streptomycin) at 37 °C in 5% CO_2. SW620 cells were cultured in complete Leibovitz's L-15 Medium (10% FBS, 2 mM glutamine, 100 μg ml^{-1} penicillin and 100 μg ml^{-1} streptomycin) in 37 °C air with no CO_2. PC9, H1975 and H1299 cells were cultured in complete RPMI (RPMI 1640 supplemented with 2 mM L-glutamine, 1 mM sodium pyruvate, 1 mM nonessential amino acids, 20 mM HEPES pH 7.5, 50 mM b-mercaptoethanol, 100 U ml^{-1} penicillin, 100 mg ml^{-1} streptomycin, 10% FBS). 293T cells were cultured in complete DMEM (10% FBS, 2 mM glutamine, 100 μg ml^{-1} penicillin and 100 μg ml^{-1} streptomycin) at 37 °C in 5% CO_2.

Human primary cell isolation and culture.

Peripheral blood mononuclear cells (PBMCs) were isolated[51], resuspended in complete RPMI medium and stimulated with soluble anti-human CD3 (10 μg ml^{-1} HIT3α) and CD28 (10 μg ml^{-1} CD28.2) antibodies for 3 d. IL-2 (100 U ml^{-1}) was then added to the medium for long-term T cell culture.

C. rodentium infectious colitis mouse model.

Littermate or cohoused *Rhbdf2*$^{-/-}$ and wild-type C57BL6/N mice were used for infection. Over three repeats, a total of 30 female and 4 male mice aged 8–15 weeks were used.

The nalidixic acid-resistant ICC169 strain of *C. rodentium* was prepared[52] and mice were infected via oral gavage with 4.5×10^9 c.f.u. of *C. rodentium* reconstituted in PBS. Body weight and fresh stool samples were examined every other day after infection. Stool samples were resuspended in 500 µl of PBS, serially diluted and plated on LB agar plates supplemented with nalidixic acid. C.f.u. were counted the next day. On day 15 after infection, mice were euthanized and the terminal colon was collected and processed for immune cell phenotyping[52]. Hematoxylin and eosin and Periodic acid–Schiff staining were done to evaluate crypto length and goblet cell counts. Each section was blinded and investigated.

Tissue processing.

Colons were collected from euthanized mice and placed into cold complete RPMI medium. Before colon processing, the mesenteric adipose tissue was removed. Following this, the colon was cut open and washed in PBS to remove feces. It was then cut horizontally into small 1–2-cm strips, and stirred continuously in complete RPMI medium with the addition of 5 mM EDTA and 0.145 mg ml^{-1} dithiothreitol for 20 min at 37 °C. The tissues were shaken vigorously in complete medium containing 500 mg ml^{-1} DNase I (Sigma-Aldrich) and 100 mg ml^{-1} Liberase TL (Roche) at 37 °C for 20–25 min. This mixture of digested colons was finally passed through 70-mm cell strainers to create a single-cell suspension, and subsequently resuspended in 4 ml of 37.5% Percoll, centrifuged at 400*g* for 5 min and washed to enrich the leukocytes.

In vitro restimulation.

Single-cell suspensions were re-stimulated in complete medium containing 50 ng ml^{-1} PMA (Sigma-Aldrich), 5 mg ml^{-1} ionomycin (Sigma-Aldrich) and a 1:1,000 dilution of GolgiPlug (BD Bioscience) for 2.5 h at 37 °C.

Flow cytometry analysis.

After surface staining, cells were fixed and permeabilized using the Foxp3/Transcription Factor Staining Buffer Set (ThermoFisher) for 1 h at 4 °C and then stained with fluorophore-conjugated antibodies overnight at 4 °C in the presence of purified anti-mouse CD16/32 and purified rat gamma globulin. Dead cells were excluded using LIVE/DEAD Fixable Blue Dead Cell Stain Kit (Invitrogen Life Technologies). Each mouse cell type was defined as follows: CD4 T cells: $CD45^+$, $Thy1.2^+$, $TCR\beta^+$, $CD4^+$ cells; CD8 T cells: $CD45^+$, $Thy1.2^+$, $TCR\beta^+$, $CD8^+$ cells; eosinophils: $CD45^+$, $Linage\ marker^+$, $CD11b^+$ cells; neutrophils: $CD45^+$, $lineage\ marker^-$, $Ly6G^{high}$, $CD11b^+$ cells; dendritic cells: $CD45^+$, $lineage\ marker^-$, $Ly6G^{intermediate}$, $CD11c^+$, $MHC\text{-}classII^+$ cells; macrophages: $CD45^+$, $linage\ marker^-$, $Ly6G^{intermediate}$, $CD64^+$, $CCR2^+$, $MHC\text{-}classII^+$ cells. The gating strategy is shown in Extended Data Fig. 6.

Fecal microbiome metagenomics and analysis.

Fecal microbiome was analyzed as previously described[53]. DNA was isolated using the MagAttract PowerMicrobiome DNA/RNA EP Kit (Qiagen) in an Eppendorf epMotion 5073 automated liquid handling system. Metagenomic libraries were prepared using 30 µl of DNA

with the Nextera DNA Flex Library Prep Kit (Illumina). Library preparation was initiated with tagmentation and post-tagmentation cleanup followed by amplification of tagmented DNA and cleanup using Sample Purification Beads for both cleanup steps. The individual libraries were diluted and pooled at a concentration of 7 nM to make the final library. This pool was normalized to 1.8 pM, spiked-in with 1% PhiX sequencing control and sequenced on an Illumina NextSeq 500 instrument. For sequence analysis, MetaPhlAn2 was used to obtain relative abundances. Principal coordinates analysis plots were generated using the Canberra distance metric based on resulting species-level classifications[54]. For estimating percentages of Human Microbiome Project (HMP) body site origin, the SourceTracker[55] approach was applied by training on MetaPhlAn data from the HMP. Alpha values were tuned via cross-validation, and SourceTracker analyses were performed on genus-level taxonomic classifications.

P. aeruginosa infectious pneumonia mouse model.

Rhbdf2$^{-/-}$ and wild-type C57BL6/N mice were used for three repeats of this infection, with 26 male and 9 female mice all aged 8–15 weeks old. Mice were age-matched for each repeat. *P. aeruginosa* (HER-1018) bacterial cultures were grown in LB Soy Agar, spun down and resuspended in PBS to a concentration of 1.25×10^{10} c.f.u. per ml. *Rhbdf2*$^{-/-}$ and wild-type mice were inoculated with 40 µl of this solution via a nasal gavage under anesthesia. Following infection, the mice were weighed each day. On day 3, the mice were euthanized, and their lungs were collected and disaggregated with a 70-µM cell strainer in 4 ml of PBS. Each solution was serially diluted and plated on a blood agar plate. C.f.u. were counted following 24 h.

Generation of iRHOM2 antibody.

In collaboration with R&D systems, mice were immunized with a peptide generated against human iRHOM2 (amino acids: 93–107; sequence: EPRSRWQESSEKRPG). Mouse splenocytes were isolated 17 d after immunization and fused with myeloma cells. Hybridomas were screened by ELISA and subcloned to single-cell monoclonals grown for pilot lots. Antibodies were purified using Protein G and quality testing was performed using size-exclusion HPLC.

Mouse lung epithelial cell isolation.

As previously described[56], mice were killed through intraperitoneal injection of ketamine/xylazine and exsanguinated, and their lungs were perfused with 10 ml of PBS. Dispase (3–5 ml, 5,000 units per ml, Corning) was instilled in the lungs, the trachea was closed with suture thread and lungs were removed and placed in 1 ml of dispase and incubated for 12 min in a 37 °C water bath. Lobes were dissected and placed in a C-tube containing 5 ml of cRPMI medium and 10 Kunitz units per ml of DNAse (Sigma). The lungs were dissociated twice using program ‘m_lung_1.01’ on the GentleMACs Dissociator (Miltenyi Biotec). Lung cells were resuspended in MACS buffer (0.5% BSA, 2 mM EDTA in PBS) and incubated with anti-mouse CD16/32 blocking antibody (1:100, BioLegend) for 10 min at 4 °C, and then biotinylated anti-mouse CD45 (1:100 µl, clone: 30-F11, BioLegend), CD31 (1:200 µl, clone: MEC13.3, BioLegend), TER119 (1:200 µl, clone: TER119, BioLegend) and CD90 (1:200 µl, clone: 53–2.1, BioLegend) antibodies were added and incubated at

4 °C for 30 min. Cells were then incubated with biotin Microbeads (Miltenyi Biotec) at 4 °C for 15 min, before being added to a rinsed LS Column (Miltenyi Biotec). Eluent (lung epithelial cells) was collected and stained with AF700 anti-mouse CD45 (1:100, clone: 104, eBioscience) and PE anti-mouse CD326 (1:100, clone: G8.8, BioLegend) antibodies, and fixable viability dye eFluor780 (1:1,500, eBioscience). Cells were fixed with 2% paraformaldehyde for 15 min and analyzed by flow cytometry to assess purity.

Next-generation sequencing.

Genomic DNA was isolated from PBMCs using the DNeasy Blood and Tissue Kit (Qiagen) per the manufacturer's instructions. Whole genome (family 2) or whole exome (family 1) sequencing was performed on genomic DNA using the Illumina HiSeq sequencing system. The sequenced DNA reads were mapped to the hg19 human genome reference using the Burrows–Wheeler Aligner with default parameters. Variant calling was performed using the Genome Analysis Toolkit v.3.4 (Broad Institute) and annotated by variant effect predictor and prioritized by GEMINI (Genome MINIng) based on population allele frequency, functional prediction and genetic models.

siRNA knockdown.

T cells were resuspended in high-efficiency buffer (140 mM sodium phosphate (pH 7.2), 5 mM KCl and 10 mM $MgCl_2$) with siRNA (Trilencer-27 Human siRNA, Origene). Cells were transferred to Nucleocuvettes (Lonza) and electroporated using program EO-115 on the Amaxa Nucleofector 96-well Shuttle System (Lonza). After electroporation, cells were transferred to prewarmed complete medium.

A549 cells (1×10^5 cells per well) were seeded in a 12-well plate containing complete medium and transfected with siRNA using siLentfect Lipid (BioRad) reagent. To quantify AREG secretion, medium was replaced 48 h following lipofection and collected 24 h later, for analysis by the Human Amphiregulin DuoSet ELISA (R&D Systems).

Luminex assays.

The Cytokine/Chemokine/Growth Factor 48-Plex Human panel (Invitrogen, ThermoFisher) was carried out on plasma according to the manufacturer's instructions.

CRISPR–Cas9 knockout.

Cells were resuspended in high-efficiency buffer, with a crRNA and tracrRNA (Integrated DNA Technologies) complex and Cas9 protein (ThermoFisher). Cells were electroporated in nucleocuvettes (Lonza) using program EH-100 on the Amaxa Nucleofector 96-well Shuttle System (Lonza), and transferred to prewarmed complete medium.

Overexpression of iRHOM2.

The lentiviral iRHOM2 plasmid was generated from pLV-EF1a-IRES-Puro (Addgene) vector by replacing the puromycin fragment with a truncated EGFR protein. PCR-amplified DNA fragments were cloned into the recipient vector via an In-Fusion cloning (Takara Bio) procedure. The product was transformed using Stellar competent cells (Takara Bio) and plated on ampicillin agar plates (100 μg ml^{-1}). The plasmid was verified by Sanger

sequencing. The lentiviral iRHOM2 plasmid and plasmids containing PAX2 and VSV-G (Addgene) were transfected into 293T cells using Lipofectamine 3000 reagent (Invitrogen). Culture supernatants containing lentivirus were collected at day 2 and concentrated by Lenti-X Concentrator (Takara Bio). For iRHOM2 overexpression, human PBMCs following 24-h TCR stimulation were cultured with Polybrene (Sigma) and lentivirus.

Quantitative PCR with reverse transcription.

RNA was isolated using the RNeasy Plus Mini Plus Kit (Qiagen) and complementary DNA was synthesized from RNA using the iScript cDNA Synthesis Kit (BioRad). Quantitative PCR with reverse transcription was performed using the standard ABI System with 25 ng of cDNA, TaqMan Universal PCR Master Mix and TaqMan Gene Expression Assays. The following TaqMan Gene Expression Assays were used for PCR analysis: *RHBDF1* (Hs.PT.58.40446979, exons 3–4, Integrated DNA Technologies), *RHBDF2* (Hs00226277_m1, exons 11–12, Applied Biosystems), *ADAM17* (Hs. PT.58.40361975, exons 12–13, Integrated DNA Technologies) and 18S (Eukaryotic 18S) (Applied Biosystems). Relative quantifications of mRNAs were calculated by the double delta cycle threshold method.

Immunoblot.

Cells were lysed in Triton X-100 lysis buffer containing Complete Mini EDTA-free Protease Inhibitor Cocktail (Sigma), Phosphatase Inhibitor Cocktail (Sigma) and 10 mM 1,10-phenanthroline. Lysates were standardized using the BCA Protein Assay Kit (Pierce). Proteins were resolved by SDS–PAGE, transferred onto nitrocellulose membranes and blocked in TBS-T (Tris-buffered saline, 0.1% Tween-20) containing 5% milk before primary antibody incubation.

Membrane TNF assay and TNF ELISA.

Primary T cells were stimulated for 4 h at 37 °C by plate-bound anti-human CD3 antibody (HIT3a, BioLegend). APC anti-human TNF antibody (1:200, Mab11, BioLegend) was added to the cells during stimulation. Cells were collected, washed with FACS buffer (2% FBS and 0.05% NaN_3 in PBS) and stained for Pacific Blue or BV421 anti-human CD2 antibody (TS1/8, BioLegend) and fixable viability dye eFluor780 (1:1,500, eBioscience). Cells were fixed with 2% paraformaldehyde for 15 min and analyzed by flow cytometry. For iRHOM2-overexpressed cells, anti-EGFR antibody (1:200, R&D Systems) was used to gate transduced cells. Cell culture supernatants were collected following stimulation, and TNF was measured using the human TNF ELISA Set (BD OptEIA, BD Biosciences). $CD14^+$ monocytes were isolated from PBMCs using the Miltenyi Pan Monocyte Isolation Kit and then stimulated for 4 h with 125 ng ml^{-1} LPS cRPMI. mTNF levels were measured as described above.

Legendplex bead-based multiplex assay.

For measurements of cytokines, chemokines and growth factors in patient serum and cell culture supernatant, the Legendplex Panel (BioLegend) was used. Measurements were taken on a flow cytometer.

sgRNA knockout.

iRHOM1, iRHOM2, AREG, HB-EGF and TGF-α knockout plasmids were generated from the lentiCRISPRv2 vector (Addgene). PCR-amplified DNA fragments were cloned into the recipient vector via an In-Fusion cloning (Takara Bio) procedure. The product was transformed using Stellar competent cells (Takara Bio) and plated on ampicillin agar plates (100 μg ml^{-1}). The plasmid was verified by Sanger sequencing. Knockout plasmids and plasmids containing PAX2 and VSV-G (Addgene) were transfected into 293T cells using Lipofectamine 3000 reagent (Invitrogen). The culture supernatants containing lentivirus were collected at day 2 and concentrated by Lenti-X Concentrator (Takara Bio). Cell lines were seeded in six-well plates in complete medium supplemented with Polybrene (Sigma) and lentiviruses. Cells were selected by puromycin.

Scratch assay.

Knocked out cells were seeded in a 12-well plate. The following day, a scratch was made with a pipette tip. The well was washed with PBS which was then replaced with fresh medium containing human AREG (50 ng ml^{-1}), TGF-α (50 ng ml^{-1}) and HB-EGF (50 ng ml^{-1}). Pictures were taken immediately after scratches were made and then 48 h later using the EVOS FL Cell Imaging System (Life Technologies) under a ×10 objective.

Single-cell data analysis.

Publicly available scRNA-seq raw count data from PBMCs were acquired from the GEO database, with accession number GSE149689 (ref.[57]). The dataset was analyzed using the Seurat package in R v.4.0.0. The data were log-normalized and scaled using default settings. We grouped the cells using *k*-nearest neighbor on the top 20 dimensions from PCA. The cells were clustered using the Louvain algorithm with a resolution of 0.5 and projected into a two-dimensional space using Uniform Manifold Approximation and Projection (UMAP).

Whole-blood mRNA sequencing (mRNA-seq).

Total RNA from whole blood was extracted using the PAXgene Blood RNA Kit (PreAnalytiX) and used to prepare RNA-seq libraries with the Illumina TruSeq Stranded mRNA library preparation kit. The mRNA-seq libraries were batched and sequence-multiplexed to an average of 50 million reads per library on the Illumina HiSeq platform. Reads were mapped to the human genome GRCh37.p13 (Genome Reference Consortium Human Reference[37]), INSDC Assembly GCA_000001405.14, Feb 2009, using STAR_2.6.1d aligner. FeatureCounts v.2.0.0 was used to generate the raw counts. Sample transcriptome data quality was assessed by evaluating homogeneity and similarity between samples. We used variance stabilizing transformation (vst) and regularized log transformation (rlog) functions (DESeq2 package v.1.26.0) to transform the raw count data, and dist function to calculate sample-to-sample distances. We plotted heatmaps of the distance matrix along with a PCA of the 1,000 most variable/most expressed genes to identify and exclude outlier samples. We used DESeq2 (v.1.26.0) to normalize the raw count matrix according to sequencing depth and RNA composition (median of ratios method) to perform differential expression. GSEA was performed using the WEB-based Gene SeT Analysis Toolkit (WebGestalt)[58]. The list of enriched differentially-expressed

genes (adjusted $P < 0.05$) and the corresponding $\log_2$ fold-change were uploaded into WebGestalt using the following parameters: minimum number of genes per category = 5; maximum number of genes per category = 2,000; significance level = false discovery rate < 0.05; number of permutations = 1,000; $P = 1$; collapse method = mean; number of categories expected from set cover = 10; number of categories visualized in the report = 40; color in DAG = continuous. Affinity propagation to condense gene sets in the enrichment result was run as a post-processing step to identify the most representative sets with low redundancy for visualization.

mRNA-seq of activated T cells.

Expanded primary T cells were stimulated with 20 ng ml^{-1} PMA and 450 μg ml^{-1} ionomycin in cRPMI. Cells were collected at 3 h and 6 h post-stimulation and frozen at −80 °C. The remaining cells were washed to remove residual PMA/ionomycin and continue culturing. Cells were collected at 12 h and 21 h post-stimulation and frozen. RNA was isolated using the RNeasy Plus Micro Kit (Qiagen). Reverse transcription, cDNA preamplification and sequencing library preparation were performed[59]. Multiplexed libraries were pooled and paired-end 150-base-pair sequencing was performed on the Illumina HiSeq platform at Sidra Medicine. Sequenced libraries yielded an average of 20 million reads per library. Reads were mapped and raw counts generated for the whole-blood mRNA-seq. Transcriptome data quality was assessed and outlier samples identified and excluded. Count normalization and differential expression analysis was done using DEseq2 package (v.1.26.0). Cluster analysis was performed using the data from the HC T cells with GSEA and affinity propagation performed in each cluster. Comparison between HC and patient T cells was further performed using the mean expression of each cluster.

Cluster analysis and PCA.

Cluster analyses were performed by the Ward method, using multi-omics data. Each horizontal row shows the normalized expression per one gene among patients and HCs at different time points, with a color scale indicating expression strength. PCA was performed to statistically aggregate items, reducing the number of observed variables and reducing the dimensionality of omics data.

Enrichment map using RNA-seq data.

We performed gene ontology (GO) enrichment using ToppGene[60]. GO terms were displayed using cut-off value false discovery rate < 0.000001 as an enrichment map. Cytoscape v.3.8.2 was used to draw edges between overlapping nodes/functions.

Calculation of HIES score.

A HIES scoring system developed for genetic linkage studies[27] was used for the screening of autosomal-dominant HIES. HIES is considered highly likely with a score of >40 and unlikely with a score of <20 points. A score between 20 and 40 has intermediate probability.

Lipidomics.

Cells were washed with 0.9% NaCl in HPLC-grade water and resuspended in HPLC-grade methanol. HPLC water and chloroform with 1% ethanol as stabilizer were added, and the samples were shaken for 60 min at 4 °C, and centrifuged at 20,000*g* for 20 min. The resulting organic layer containing lipids was extracted and dried by vacuum, before resuspension in 6:1 isopropanol/methanol with butylated hydroxytoluene. These samples were run on a mass spectrometer and the data were annotated by Metaboscape (Bruker).

Statistical analysis.

Data are represented as mean ± s.d. and were analyzed by two-tailed, unpaired Student's *t*-test unless stated otherwise.

Reporting Summary.

Further information on research design is available in the Nature Research Reporting Summary linked to this article.

Extended Data

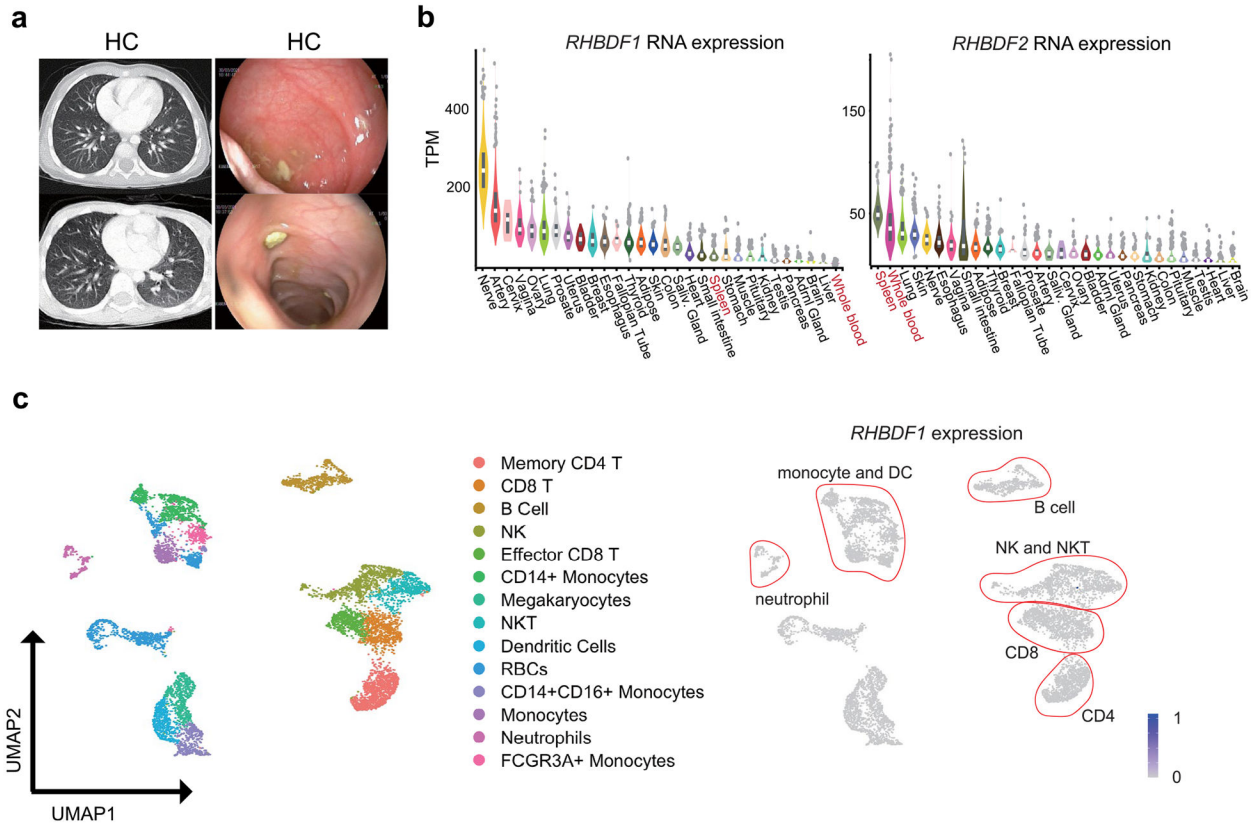

Extended Data Fig. 1 |. Disease and RHBDF expression.

(a) (left) Thoracic computed tomography (CT) scan in healthy control. (right) Photographs of the mucosa from lower G.I. endoscopy in healthy control. **(b)** RNA−seq data (GTEx Portal https://www.gtexportal.org) showing RHBDF2 expression across organs. **(c)**

RHBDF1 expression in peripheral blood cell-types. Data are derived from the single cell RNA-seq dataset from the GEO database, accession number GSE149689. The clusters were projected into a 2-dimensional space using uniform manifold approximation and projection (UMAP) and identified using (left panel) canonical markers, and (right panel) RHBDF1 expression in individual cells. Color intensity indicates the expression level.

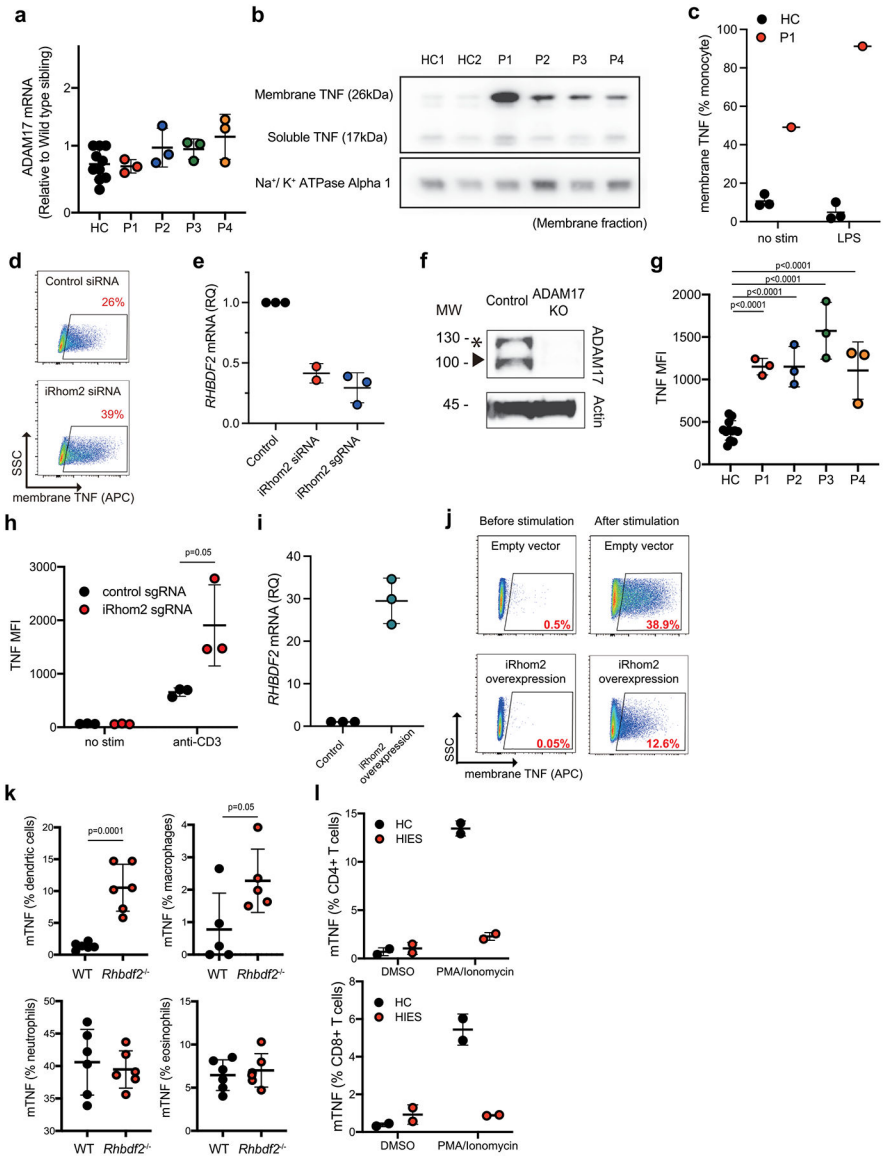

Extended Data Fig. 2 |. iRHOM2 deficiency impairs ADAM17-dependent TNF shedding.
(**a**) Quantitative RT-PCR (Q-PCR) of *ADAM17* mRNA isolated from healthy control (HC) and patient (P) T cells. β-actin, GAPDH, or 18 S served as the endogenous control. Data of three independent experiments. **(b)** Western blot of TNF and Na +/K + ATPase Alpha 1 expression in membrane fractions of patient and healthy T cells stimulated with anti-CD3 for four hours. **(c)** Membrane TNF on live-gated $CD14^{+}$ monocytes from HCs and P1 either untreated or stimulated with lipopolysaccharide (LPS) for 4 hours measured as in Fig. 1 (n

= 4 for HC group). **(d)** Flow cytometry as in b, for HC cells either with or without treating with control or iRhom2 (RHBDF2)-targeting small interfering RNAs (siRNAs) as indicated. **(e)** Knockdown and knockout efficiency are shown by Q-PCR of *RHBDF2* using RNA isolated from T cells. β−actin was the endogenous control. RQ, relative quantitation (n = 3 per group). **(f)** Knockout efficiency shown by western blot of ADAM17 and β-actin loading control using T cells from HC. Asterisk, pro-ADAM17; arrowhead, mature ADAM17. **(g)** mTNF (mean fluorescence intensity) MFI for T cells from HC and Ps stimulated with anti-CD3 antibody. Data of three independent experiments. **(h)** mTNF MFI for HC T cells treated with control sgRNA and iRHOM2 sgRNA and the stimulated with 10 μg/ml anti-CD3 antibody for 4 hours (n = 3 per group). **(i)** Q-PCR of *RHBDF2* mRNA isolated from T cells treated with negative (control) or wild-type *RHBDF2* coding sequence. RNA was isolated 5 days after lentiviral transduction. β−actin was the endogenous control (n = 3 per group). **(j)** Flow cytometry dot plots of cell side scatter (SSC) mTNF expression (percentage given in the expression gate) by live $CD2^+$ HC T cells transduced with empty or iRHOM2 overexpressing lentiviral vector and then stimulated with anti-CD3 (10 μg/ml) for 4 hours. **(k)** Flow cytometric mTNF measurements from isolated cell populations from either WT or $Rhbdf2^{-/-}$ mice (Gating strategy was shown in Extended Data Fig. 6); Error bars represent standard error of the mean (n = 6 per group). (**l**) CD4 T cells (upper panel) and naïve CD8 T cells (lower panel) from HC and STAT3-deficient HIES patients stimulated with PMA (20 ng/ml) and ionomycin (750 ng/ml) or dimethyl sulfoxide (DMSO) vehicle for 4 hours and analyzed. Scatter plots were generated by gating on live $CD3^+CD4^+$, $CD3^+CD8^+$, $CD4^+$, or $CD8^+$ T cells (n = 2 per group). All data are mean ± s.d. and were analyzed by two-tailed, unpaired Student's t-test (**g**, **h**, **k**).

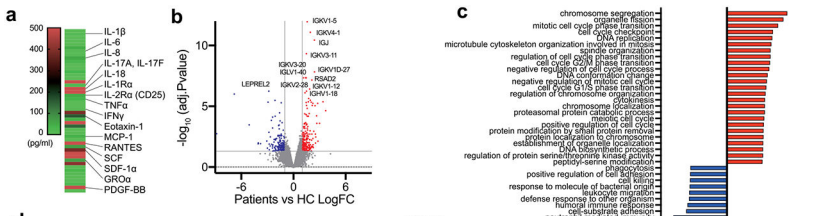

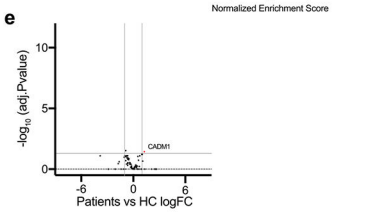

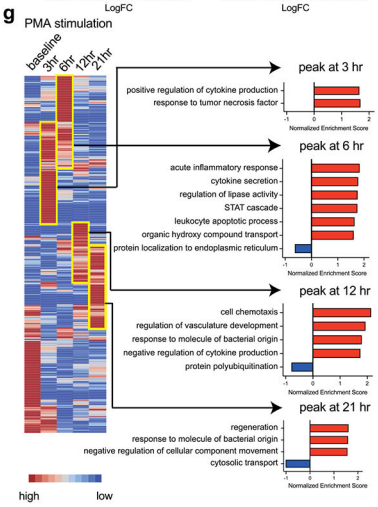

d

Protein name	gene name	log$_2$FC	p-value	adjusted p-value
Angiotensin Converting Enzyme 2	ACE2	0.91	0.80	NA
Activated Leukocyte Cell Adhesion Molecule	ALCAM	0.14	0.58	0.76
Amyloid Beta Precursor Like Protein 2	APLP2	-0.65	0.01	0.08
Amyloid Beta Precursor Protein	APP	-0.27	0.17	0.39
Amphiregulin	AREG	-2.08	0.55	NA
AXL Receptor Tyrosine Kinase	AXL	-0.79	0.16	0.38
Carbonic Anhydrase 9	CA9	0.11	0.96	NA
Cell Adhesion Molecule 1	CADM1	1.27	0.00	0.04
CD163 Molecule	CD163	-0.89	0.01	0.09
Programmed Cell Death 1 Ligand 1	CD274	1.03	0.00	0.06
CD40 Molecule	CD40	0.30	0.29	0.53
CD44 Molecule	CD44	0.13	0.43	0.65
Collagen Type XVII Alpha 1 Chain	COL17A1	-3.82	0.01	0.08
Colony Stimulating Factor 1	CSF1	-0.08	0.79	0.89
Colony Stimulating Factor 1 Receptor	CSF1R	-0.41	0.09	0.28
Cystatin C	CST3	-0.81	0.01	0.08
Cullin 5	CUL5	0.74	0.01	0.08
IL-8	CXCL8	-1.74	0.14	0.35
Delta Like Non-Canonical Notch Ligand 1	DLK1	-2.87	0.41	NA
Delta Like Canonical Notch Ligand 1	DLL1	1.07	0.06	0.22
Desmoglein 2	DSG2	2.46	0.20	NA
Epithelial Cell Adhesion Molecule	EPCAM	2.69	0.32	NA
Epithelial Mitogen	EPGN	0.13	0.97	NA
Epiregulin	EREG	0.65	0.40	NA
F11 Receptor	F11R	-0.70	0.01	0.08
Fc Fragment Of IgA Receptor	FCAR	-0.30	0.51	0.71
Fc Fragment Of IgG Receptor IIIa	FCGR3A	-0.08	0.76	0.88
Glycoprotein Ib Platelet Subunit Alpha	GP1BA	-0.64	0.13	0.35
Glycoprotein V Platele	GP5	-0.30	0.48	0.69
Glycoprotein VI Platelet	GP6	0.46	0.32	0.56
Hepatitis A Virus Cellular Receptor 1	HAVCR1	0.47	0.51	NA
Hepatitis A Virus Cellular Receptor 2	HAVCR2	0.27	0.23	0.47
Heparin Binding EGF Like Growth Factor	HBEGF	0.32	0.45	0.66
Intercellular Adhesion Molecule 1	ICAM1	-0.53	0.04	0.17
Inducible T Cell Costimulator Ligand	ICOSLG	0.08	0.74	0.86
Insulin Like Growth Factor 2 Receptor	IGF2R	-0.74	0.02	0.12
Interleukin 15 Receptor Subunit Alpha	IL15RA	0.30	0.23	0.46
Interleukin 1 Receptor Type 2	IL1R2	-0.97	0.01	0.08
Interleukin 6 Receptor	IL6R	-0.58	0.03	0.14
Jagged Canonical Notch Ligand 1	JAG1	0.37	0.56	0.75
KIT Ligand	KITLG	1.31	0.60	NA
Klotho	KL	0.08	0.94	NA
L1 Cell Adhesion Molecule	L1CAM	-0.88	0.05	0.20
Lymphocyte Activating 3	LAG3	0.27	0.36	0.59
Low Density Lipoprotein Receptor	LDLR	0.52	0.01	0.09
LDL Receptor Related Protein 1	LRP1	-0.71	0.02	0.13
Lymphotoxin _	LTA	-0.38	0.11	0.31
LY6/PLAUR Domain Containing 3	LYPD3	-1.05	0.01	0.10
MHC Class I Polypeptide-Related Sequence A	MICA	-0.42	0.16	0.37
MHC Class I Polypeptide-Related Sequence B	MICB	0.03	0.89	0.95
Mucin 1	MUC1	-0.62	0.10	0.29
Neural Cell Adhesion Molecule 1	NCAM1	0.06	0.83	0.91
Nectin Cell Adhesion Molecule 4	NECTIN4	0.59	0.04	0.19
Notch Receptor 1	NOTCH1	-0.58	0.02	0.13
Neuregulin 1	NRG1	-1.64	0.07	0.24
Neuropilin 1	NRP1	-0.66	0.25	0.49
Neurotrophic Receptor Tyrosine Kinase 1	NTRK1	0.69	0.36	0.59
Procollagen C-Endopeptidase Enhancer	PCOLCE	-0.32	0.18	0.40
Premelanosome Protein	PMEL	-0.98	0.26	NA
Prion protein	PRNP	0.02	0.92	0.96
Protein C Receptor	PROCR	-0.18	0.63	0.80
Protein Tyrosine Kinase 7	PTK7	0.98	0.00	0.06
Protein Tyrosine Phosphatase Receptor Type F	PTPRF	-1.15	0.07	NA
Scribble Planar Cell Polarity Protein	SCRIB	-0.21	0.31	0.55
Syndecan 1	SDC1	2.55	0.00	NA
Syndecan 4	SDC4	-0.25	0.49	0.70
Selectin L	SELL	0.09	0.70	0.84
Semaphorin 4D	SEMA4D	-0.51	0.02	0.14
Sortilin Related VPS10 Domain Containing Receptor 3	SORCS3	-1.22	0.29	NA
Sortilin Related Receptor 1	SORL1	-0.66	0.02	0.12
Sortilin 1	SORT1	-0.39	0.15	0.36
Transforming Growth Factor Alpha	TGFA	-0.21	0.56	0.75
Thrombospondin 4	THBS4	0.04	0.95	0.97
T Cell Immunoglobulin And Mucin Domain Containing 4	TIMD4	0.34	0.51	0.71
Tumor Necrosis Factor	TNF	-0.22	0.41	0.64
TNF Receptor Superfamily Member 1A	TNFRSF1A	-0.77	0.01	0.08
TNF Receptor Superfamily Member 1B	TNFRSF1B	-0.87	0.00	0.03
TNF Receptor Superfamily Member 8	TNFRSF8	-0.64	0.03	0.15
RANKL	TNFSF11	2.11	0.19	NA
Triggering Receptor Expressed On Myeloid Cells 2	TREM2	-1.42	0.10	NA
Vasorin	VASN	0.48	0.79	NA
Fractalkine	CX3CL1		no expression	
Erb-B2 Receptor Tyrosine Kinase 4	ERBB4		no expression	
Growth Hormone Releasing Hormone Receptor	GHRHR		no expression	
Kinase Insert Domain Receptor	KDR		no expression	
Natriuretic Peptide Receptor 1	NPR1		no expression	
Protein Tyrosine Phosphatase Receptor Type Z1	PTPRZ1		no expression	
Sortilin Related VPS10 Domain Containing Receptor 1	SORCS1		no expression	

Extended Data Fig. 3 |. Cytokine and mRNA changes associated with iRHOM2 deficiency.
(a) Heat map of multiplex measurements of 48 cytokine levels in HC plasma using the Luminex system. **(b)** Volcano plot of whole blood RNA-seq showing upregulated genes (red) and down regulated genes (blue) in the patient sample from iRHOM2 deficient patients compared to HC. **(c)** GSEA based on the patient whole blood RNA-seq data in comparison to healthy control. NES; normalized enrichment score. **(d)** Table of ADAM17 regulated molecules extracted from whole blood RNA-seq. **(e)** Volcano plot of gene expression with fold difference between $\log_2$ normalized expression shown in Fig. 5d versus $-\log_{10}$ adjusted P-value in whole blood. Vertical grey lines indicate fold changes, with a cut off ±2. The horizontal line represents a p-value of 1^{-10}. **(f)** Similar with Fig. 5f, volcano plot of gene expression before and after 3 hours stimulation in T cells from 4 HC (left panel) and 4 patients (right panel). Red dots represent upregulated mRNAs and blue dots indicate downregulated mRNAs. **(g)** Hierarchical clustering of stimulated T cells RNA-seq data

in the different time points using HC samples. Time is shown on the x-axis and gene expression levels are shown on the y-axis. Mean expression was used from 4 HC samples. Statistical significance was calculated by using the Wald test for hypothesis testing (**b**, **e**, **f**).

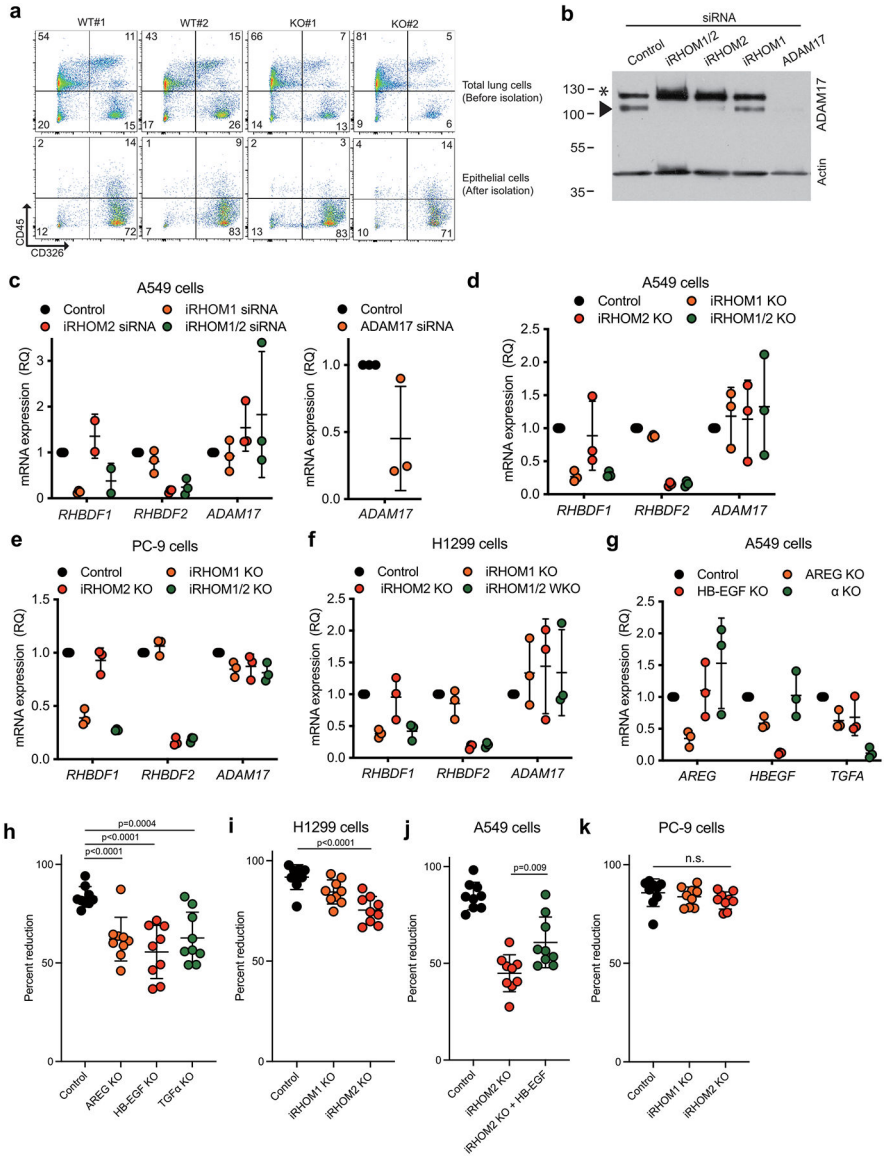

Extended Data Fig. 4 |. Loss of iRHOM2 in lung epithelial cells affects ADAM17 maturation/ activity.

(a) Flow cytometry dot plots confirming the enrichment of mouse non-hematopoietic CD326^{+} epithelial cells isolated from total lung cells from two wild type (WT) or *Rhbdf2*$^{-/-}$ (KO) mice by magnetic separation. CD45, hematopoietic cell marker; CD326, epithelial cell marker. **(b)** Western blot as in Fig. 4 g, of A549 lung tumor cells treated with the indicated siRNA. **(c)** Q-PCR of *RHBDF1*, *RHBDF2* and *ADAM17* in A549 cells treated with the indicated siRNAs or control RNA for 48 hours. RQ, relative quantitation. Data of three independent experiments (n = 3 per group). **(d)** Q-PCR as in (c), in A549 cells (n = 3 per group). **(e)** Q-PCR as in (c), in H1299 cells (n = 3 per group). **(f)** Q-PCR as in (c), in PC9

cells (n = 3 per group). **(g)** Q-PCR of *AREG*, *HBEGF* and *TGFA* in A549 cells knocked out of indicated targets (n = 3 per group). **(h)** Wound healing assay as in Fig. 4j, in knockout of indicated targets in A549 cells (n = 3 per group). **(i)** Wound healing assay as in Fig. 4j, in knockout H1299 cells either with or without HB-EGF (n = 9 per group). **(j)** Wound healing assay as in Fig. 4i, in knockout A549 cells (n = 9 per group). **(k)** Wound healing assay as in Fig. 4i, in knockout PC9 cells (n = 9 per group). All data are mean ± s.d. and were analyzed by two-tailed, unpaired Student's t-test (**h**-**k**).

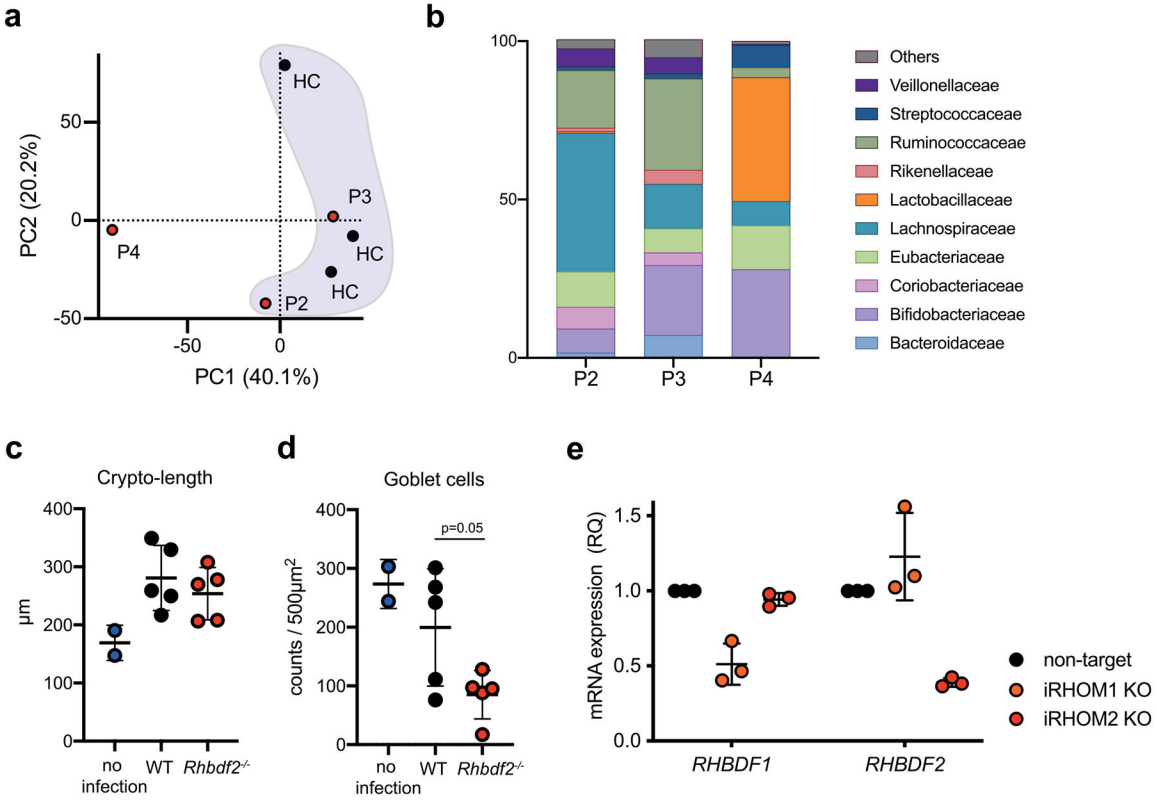

Extended Data Fig. 5 |. Loss of iRHOM2 in colon epithelial cells is compensated for by iRHOM1 expression.

(a) Scatter plot of principal coordinates analysis axis one (PC1) and axis two (PC2) performed on North American healthy control and patients' microbiome profiles. Individual data points are colored according to patients and HC. **(b)** Composition of microbes in patient stool organized by identified families of bacteria **(c)** Crypt length in colons of mice with and without infection by *C. rodentium* (n = 3 for each WT and KO groups). **(d)** The number of goblet cells in 500 µm^2 in colons of mice (n = 3 for each WT and KO groups). **(e)** Q-PCR of *RHBDF1* and *RHBDF2* in SW620 cells treated with the indicated sgRNAs or control RNA. 18 S was the endogenous control. RQ, relative quantitation (n = 3 per group). All data are mean ± s.d. and were analyzed by two-tailed, unpaired Student's t-test (**c**-**e**).

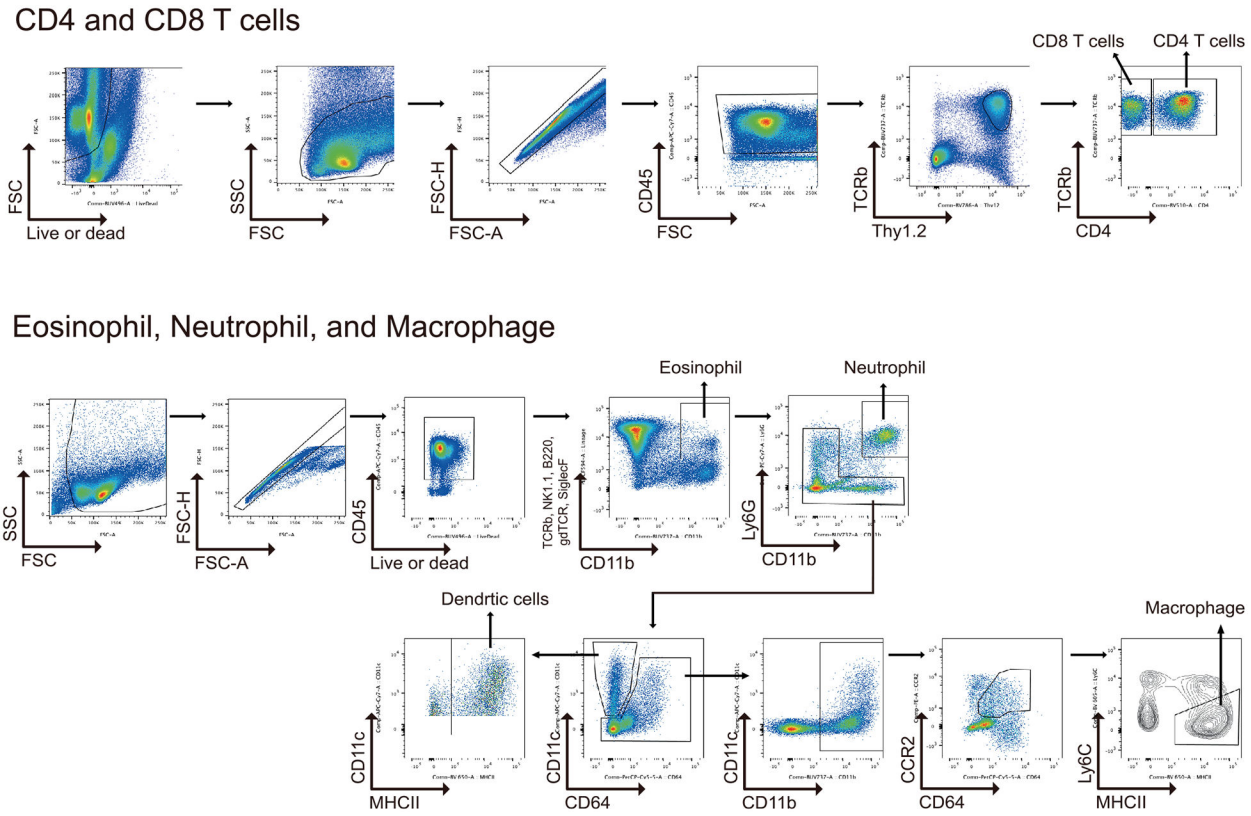

Extended Data Fig. 6 |. Gating strategy for detecting T cells, eosinophils, neutrophils, and macrophages.

Scatter plots of gating strategy are shown.

Acknowledgements

This work was supported by the Division of Intramural Research, National Institute of Allergy and Infectious Diseases, NIH, and the Sidra Medicine Internal Research Fund (grant nos. SDR400013, SDR200070). S.K. was supported by the Japan Research Foundation for Clinical Pharmacology. J.M.F. was supported by the Postdoctoral Research Associate Training Program of the National Institute of General Medical Sciences. A.D.W. was supported by the Emory University M.D./Ph.D. Program, the National Institutes of Health M.D./Ph.D. Partnerships Program, the National Institutes of Health Oxford-Cambridge Scholars Program and the International Biomedical Research Alliance. We thank K. Huang, S. Xirasagar, D. Hurt and other members of the Bioinformatics and Computational Biosciences Branch (BCBB), NIAID, and Y. Zhang for variant assessment and bioinformatics support. We also thank the Sidra Medicine pathology team, notably W. Mifsud, and the Sidra Medicine Genomics and Bioinformatics cores' teams, notably S. Lorenz, L. Mathew, L. Liu, K. Wang, F. Vempalli and G. Mubarak, for technical support. We thank H. Su, J. Milner, J. Ravell and Y. Zhang for invaluable editorial and scientific feedback. We are grateful to Merck Sharp & Dohme Corp., a subsidiary of Merck & Co., Inc., Kenilworth, NJ, USA, for generous support.

Data availability

The RNA-seq data have been deposited to the GEO database under the accession number GSE184877. WGS/WES data for the kindreds of P1 and P2 were submitted to the National Center for Biotechnology Information (NCBI) database of Genotypes and Phenotypes (dbGaP) (accession no., phs002478.v1.p1). Source data are provided with this paper.

References

1. Williams RA, Mamotte CD & Burnett JR Phenylketonuria: an inborn error of phenylalanine metabolism. Clin. Biochem. Rev 29, 31–41 (2008). [PubMed: 18566668]
2. Freeman M The rhomboid-like superfamily: molecular mechanisms and biological roles. Annu. Rev. Cell Dev. Biol 30, 235–254 (2014). [PubMed: 25062361]
3. Lambrecht BN, Vanderkerken M & Hammad H The emerging role of ADAM metalloproteinases in immunity. Nat. Rev. Immunol 18, 745–758 (2018). [PubMed: 30242265]
4. Dulloo I, Muliyil S & Freeman M The molecular, cellular and pathophysiological roles of iRhom pseudoproteases. Open Biol. 9, 190003 (2019). [PubMed: 30890028]
5. Adrain C, Zettl M, Christova Y, Taylor N & Freeman M Tumor necrosis factor signaling requires iRhom2 to promote trafficking and activation of TACE. Science 335, 225–228 (2012). [PubMed: 22246777]
6. McIlwain DR et al. iRhom2 regulation of TACE controls TNF-mediated protection against *Listeria* and responses to LPS. Science 335, 229–232 (2012). [PubMed: 22246778]
7. Cavadas M et al. Phosphorylation of iRhom2 controls stimulated proteolytic shedding by the metalloprotease ADAM17/TACE. Cell Rep. 21, 745–757 (2017). [PubMed: 29045841]
8. Grieve AG et al. Phosphorylation of iRhom2 at the plasma membrane controls mammalian TACE-dependent inflammatory and growth factor signalling. eLife 6, e23968 (2017). [PubMed: 28432785]
9. Hosur V, Farley ML, Burzenski LM, Shultz LD & Wiles MV ADAM17 is essential for ectodomain shedding of the EGF-receptor ligand amphiregulin. FEBS Open Bio 8, 702–710 (2018).
10. Zaiss DMW, Gause WC, Osborne LC & Artis D Emerging functions of amphiregulin in orchestrating immunity, inflammation, and tissue repair. Immunity 42, 216–226 (2015). [PubMed: 25692699]
11. Christova Y, Adrain C, Bambrough P, Ibrahim A & Freeman M Mammalian iRhoms have distinct physiological functions including an essential role in TACE regulation. EMBO Rep. 14, 884–890 (2013). [PubMed: 23969955]
12. Li X et al. iRhoms 1 and 2 are essential upstream regulators of ADAM17-dependent EGFR signaling. Proc. Natl Acad. Sci. USA 112, 6080–6085 (2015). [PubMed: 25918388]
13. Su AI et al. A gene atlas of the mouse and human protein-encoding transcriptomes. Proc. Natl Acad. Sci. USA 101, 6062–6067 (2004). [PubMed: 15075390]
14. Issuree PD et al. iRHOM2 is a critical pathogenic mediator of inflammatory arthritis. J. Clin. Invest 123, 928–932 (2013). [PubMed: 23348744]
15. Qing X et al. iRhom2 promotes lupus nephritis through TNF-α and EGFR signaling. J. Clin. Invest 128, 1397–1412 (2018). [PubMed: 29369823]
16. Chenxu G et al. iRhom2 loss alleviates renal injury in long-term PM2.5-exposed mice by suppression of inflammation and oxidative stress. Redox Biol. 19, 147–157 (2018). [PubMed: 30165303]
17. Kim JH et al. Role of iRhom2 in intestinal ischemia-reperfusion-mediated acute lung injury. Sci. Rep 8, 3797 (2018). [PubMed: 29491382]
18. Luo WW et al. iRhom2 is essential for innate immunity to DNA viruses by mediating trafficking and stability of the adaptor STING. Nat. Immunol 17, 1057–1066 (2016). [PubMed: 27428826]
19. Luo WW et al. iRhom2 is essential for innate immunity to RNA virus by antagonizing ER- and mitochondria-associated degradation of VISA. PLoS Pathog. 13, e1006693 (2017). [PubMed: 29155878]
20. Blaydon DC et al. RHBDF2 mutations are associated with tylosis, a familial esophageal cancer syndrome. Am. J. Hum. Genet 90, 340–346 (2012). [PubMed: 22265016]
21. Saarinen S et al. Analysis of a Finnish family confirms RHBDF2 mutations as the underlying factor in tylosis with esophageal cancer. Fam. Cancer 11, 525–528 (2012). [PubMed: 22638770]
22. Brooke MA et al. iRHOM2-dependent regulation of ADAM17 in cutaneous disease and epidermal barrier function. Hum. Mol. Genet 23, 4064–4076 (2014). [PubMed: 24643277]

23. Hosur V et al. Rhbdf2 mutations increase its protein stability and drive EGFR hyperactivation through enhanced secretion of amphiregulin. Proc. Natl Acad. Sci. USA 111, E2200–E2209 (2014). [PubMed: 24825892]
24. Hosur V, Low BE, Shultz LD & Wiles MV Genetic deletion of amphiregulin restores the normal skin phenotype in a mouse model of the human skin disease tylosis. Biol. Open 6, 1174–1179 (2017). [PubMed: 28655741]
25. Yong PF et al. An update on the hyper-IgE syndromes. Arthritis Res. Ther 14, 228 (2012). [PubMed: 23210525]
26. Al-Shaikhly T & Ochs HD Hyper IgE syndromes: clinical and molecular characteristics. Immunol. Cell Biol 97, 368–379 (2019). [PubMed: 30264496]
27. Grimbacher B et al. Genetic linkage of hyper-IgE syndrome to chromosome 4. Am. J. Hum. Genet 65, 735–744 (1999). [PubMed: 10441580]
28. Vassalli P The pathophysiology of tumor necrosis factors. Annu. Rev. Immunol 10, 411–452 (1992). [PubMed: 1590993]
29. Black RA et al. A metalloproteinase disintegrin that releases tumour-necrosis factor-α from cells. Nature 385, 729–733 (1997). [PubMed: 9034190]
30. Moss ML et al. Cloning of a disintegrin metalloproteinase that processes precursor tumour-necrosis factor-α. Nature 385, 733–736 (1997). [PubMed: 9034191]
31. Zunke F & Rose-John S The shedding protease ADAM17: physiology and pathophysiology. Biochim. Biophys. Acta Mol. Cell Res 1864, 2059–2070 (2017). [PubMed: 28705384]
32. Dreymueller D et al. Smooth muscle cells relay acute pulmonary inflammation via distinct ADAM17/ErbB axes. J. Immunol 192, 722–731 (2014). [PubMed: 24342803]
33. Aversa G, Punnonen J & de Vries JE The 26-kD transmembrane form of tumor necrosis factor α on activated $CD4^+$ T cell clones provides a costimulatory signal for human B cell activation. J. Exp. Med 177, 1575–1585 (1993). [PubMed: 7684430]
34. Hudson DM et al. P3h3-null and Sc65-null mice phenocopy the collagen lysine under-hydroxylation and cross-linking abnormality of Ehlers–Danlos syndrome type VIA. J. Biol. Chem 292, 3877–3887 (2017). [PubMed: 28115524]
35. Tian Y et al. Cytokine secretion requires phosphatidylcholine synthesis. J. Cell Biol 181, 945–957 (2008). [PubMed: 18559668]
36. Sadikot RT, Blackwell TS, Christman JW & Prince AS Pathogen–host interactions in *Pseudomonas aeruginosa* pneumonia. Am. J. Respir. Crit. Care Med 171, 1209–1223 (2005). [PubMed: 15695491]
37. Berasain C & Avila MA Amphiregulin. Semin. Cell Dev. Biol 28, 31–41 (2014). [PubMed: 24463227]
38. Liang CC, Park AY & Guan JL In vitro scratch assay: a convenient and inexpensive method for analysis of cell migration in vitro. Nat. Protoc 2, 329–333 (2007). [PubMed: 17406593]
39. Atarashi K et al. Ectopic colonization of oral bacteria in the intestine drives TH1 cell induction and inflammation. Science 358, 359–365 (2017). [PubMed: 29051379]
40. Schirmer M et al. Compositional and temporal changes in the gut microbiome of pediatric ulcerative colitis patients are linked to disease course. Cell Host Microbe 24, 600–610 e604 (2018). [PubMed: 30308161]
41. Collins JW et al. *Citrobacter rodentium*: infection, inflammation and the microbiota. Nat. Rev. Microbiol 12, 612–623 (2014). [PubMed: 25088150]
42. Lee A, Fox JG, Otto G & Murphy J A small animal model of human *Helicobacter pylori* active chronic gastritis. Gastroenterology 99, 1315–1323 (1990). [PubMed: 2210240]
43. Marchetti M et al. Development of a mouse model of *Helicobacter pylori* infection that mimics human disease. Science 267, 1655–1658 (1995). [PubMed: 7886456]
44. Higgins LM, Frankel G, Douce G, Dougan G & MacDonald TT *Citrobacter rodentium* infection in mice elicits a mucosal Th1 cytokine response and lesions similar to those in murine inflammatory bowel disease. Infect. Immun 67, 3031–3039 (1999). [PubMed: 10338516]
45. Poholek CH et al. Noncanonical STAT3 activity sustains pathogenic Th17 proliferation and cytokine response to antigen. J. Exp. Med 217, e20191761 (2020). [PubMed: 32697822]

46. Lee PW et al. IL-23R-activated STAT3/STAT4 is essential for Th1/Th17-mediated CNS autoimmunity. JCI Insight 2, e91663 (2017). [PubMed: 28878115]
47. Zheng Y et al. TNFα promotes Th17 cell differentiation through IL-6 and IL-1β produced by monocytes in rheumatoid arthritis. J. Immunol. Res 2014, 385352 (2014). [PubMed: 25436214]
48. Fremond C et al. Membrane TNF confers protection to acute mycobacterial infection. Respir. Res 6, 136 (2005). [PubMed: 16285886]
49. Pfeffer K et al. Mice deficient for the 55 kd tumor necrosis factor receptor are resistant to endotoxic shock, yet succumb to *L. monocytogenes* infection. Cell 73, 457–467 (1993). [PubMed: 8387893]
50. Rothe J et al. Mice lacking the tumour necrosis factor receptor 1 are resistant to TNF-mediated toxicity but highly susceptible to infection by *Listeria monocytogenes*. Nature 364, 798–802 (1993). [PubMed: 8395024]
51. Cook SA et al. HEM1 deficiency disrupts mTORC2 and F-actin control in inherited immunodysregulatory disease. Science 369, 202–207 (2020). [PubMed: 32647003]
52. Crepin VF, Collins JW, Habibzay M & Frankel G *Citrobacter rodentium* mouse model of bacterial infection. Nat. Protoc 11, 1851–1876 (2016). [PubMed: 27606775]
53. Ozen A et al. Broadly effective metabolic and immune recovery with C5 inhibition in CHAPLE disease. Nat. Immunol 22, 128–139 (2021). [PubMed: 33398182]
54. Segata N et al. Metagenomic microbial community profiling using unique clade-specific marker genes. Nat. Methods 9, 811–814 (2012). [PubMed: 22688413]
55. Knights D et al. Bayesian community-wide culture-independent microbial source tracking. Nat. Methods 8, 761–763 (2011). [PubMed: 21765408]
56. Messier EM, Mason RJ & Kosmider B Efficient and rapid isolation and purification of mouse alveolar type II epithelial cells. Exp. Lung Res 38, 363–373 (2012). [PubMed: 22888851]
57. Lee JS et al. Immunophenotyping of COVID-19 and influenza highlights the role of type I interferons in development of severe COVID-19. Sci. Immunol 5, eabd1554 (2020). [PubMed: 32651212]
58. Liao Y, Wang J, Jaehnig EJ, Shi Z & Zhang B WebGestalt 2019: gene set analysis toolkit with revamped UIs and APIs. Nucleic Acids Res. 47, W199–W205 (2019). [PubMed: 31114916]
59. Saraiva LR et al. Hierarchical deconstruction of mouse olfactory sensory neurons: from whole mucosa to single-cell RNA-seq. Sci. Rep 5, 18178 (2015). [PubMed: 26670777]
60. Chen J, Bardes EE, Aronow BJ & Jegga AG ToppGene Suite for gene list enrichment analysis and candidate gene prioritization. Nucleic Acids Res. 37, W305–W311 (2009). [PubMed: 19465376]

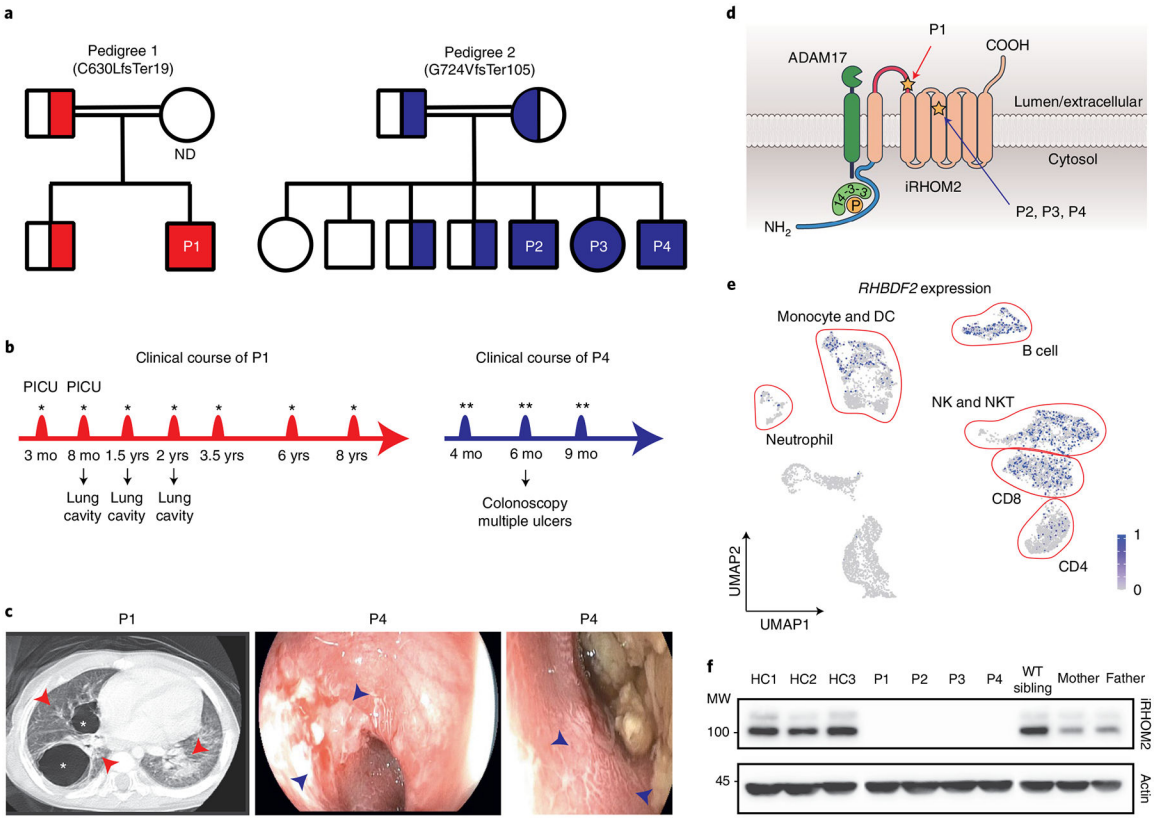

Fig. 1 |. Clinical features of iRHOM2 deficiency.

a, Pedigrees of the two kindreds: filled symbol, affected patients homozygous for the indicated mutations in *RHBDF2*; split symbols, healthy heterozygous carriers; open symbols, wild-type subjects. ND, sequence not determined. Double lines indicate consanguinity. **b**, Timelines of the clinical courses of P1 (red) and P4 (blue). Vertical hatches indicate hospitalizations; *respiratory illness; **gastrointestinal illness including diarrhea; PICU, pediatric intensive care unit. **c**, Left, thoracic computed tomography (CT) scan showing pulmonary infiltrates (red arrowheads) and pneumatoceles (asterisks) in the patient. Middle, right, photographs of the mucosa from lower gastrointestinal endoscopy. Blue arrows show mucosal ulcerations (middle) and cobblestone defects (right) in mucosa. **d**, A cartoon of human iRHOM2 associated with ADAM17 (not scaled). The N-terminal cytoplasmic domain (brown) is phosphorylated by mitogen-activated protein kinases upon stimulation, leading to recruitment of 14-3-3 proteins and activation of ADAM17 proteolytic activity. The frameshift mutations (orange stars) are within the iRHOM2 homology domain (red arrow, P1; blue arrow, P2, P3 and P4). The plasma membrane is indicated by the two scalloped borders. **e**, *RHBDF2* expression in peripheral blood cell types. Data are derived from the scRNA-seq dataset from the GEO database, accession number GSE149689. The clusters were projected into a two-dimensional space using Uniform Manifold Approximation and Projection (UMAP) and identified using (Extended Data Fig. 1c) canonical markers, and RHBDF2 expression in individual cells. Color intensity indicates the expression level. **f**, Immunoblot of iRHOM2 and β-actin loading control using patients and their family or HC T cells with locations of molecular weight (MW) markers on the

left. Representative result of two (P2 and P3) or three (others) independent experiments. DC, dendritic cell; mo, month; NKT, natural killer T; WT, wild type.

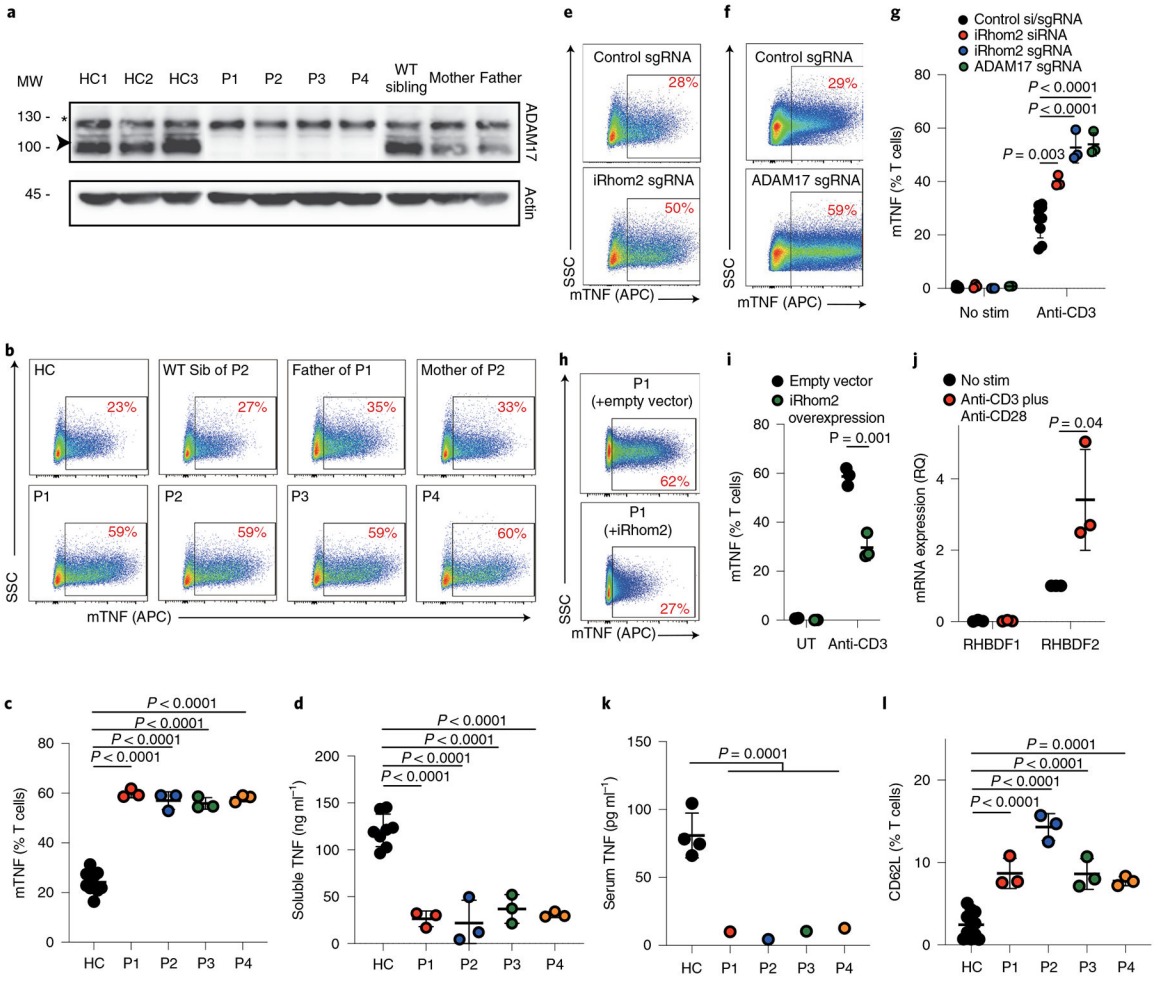

Fig. 2 |. Defective ADAM17 maturation and activity in patient T cells.

a, Immunoblot of ADAM17 and β-actin loading control using T cells from HCs, patients, WT sibling and heterozygous parents. Asterisk, pro-ADAM17; arrowhead, mature ADAM17. Representative result of three independent experiments. **b**, Flow cytometry dot plots quantitating surface mTNF expression on anti-CD3-stimulated live-gated CD2+ T cells from human subjects (patients) versus side scatter (SSC). Red, percentage of cells in positive gate. **c**, Quantification of mTNF measured in **b** ($n = 3$ per group). **d**, Level of soluble TNF in culture supernatants ($n = 3$ per group). **e**, Flow cytometry as in **b**, for HC cells with or without treatment with CRISPR–Cas9 sgRNA complexes ($n = 3$ per group). **f**, Flow cytometry as in **e**. **g**, Quantification of samples as in **e** and **f** and Extended Data Fig. 2d that were without stimulation or re-stimulated with anti-CD3 for 4 h ($n = 3$ per group). **h**, Flow cytometry as in **b**, for P1 T cells transduced with iRHOM2-expressing or empty lentiviral vectors and re-stimulated with anti-CD3 antibody for 4 h ($n = 3$ per group). **i**, Quantification of mTNF measured in **g** ($n = 3$ per group). **j**, Quantitative PCR of *RHBDF2* isolated from WT CD8 T cells and then stimulated with 10 μg ml^{-1} anti-CD3 antibody and anti-CD28 antibody for 12 h. 18S as endogenous control. RQ, relative quantitation ($n = 3$ per group). **k**, Measurements of TNF in patient or HC serum by bead-based multiplex assay ($n = 4$ for each HC and patient group). **l**, Fraction of T cells expressing CD62L in blood following

anti-CD3 stimulation for 4 h (n = 3 per group). All experiments are representative of at least two (P2 and P3) or three (others) independent experiments with similar findings. All data are mean ± s.d. and were analyzed by two-tailed, unpaired Student's t-test (**c**–**d**,**g**,**i**–**l**). APC, Allophycocyanin; stim, stimulation; UT, untreated.

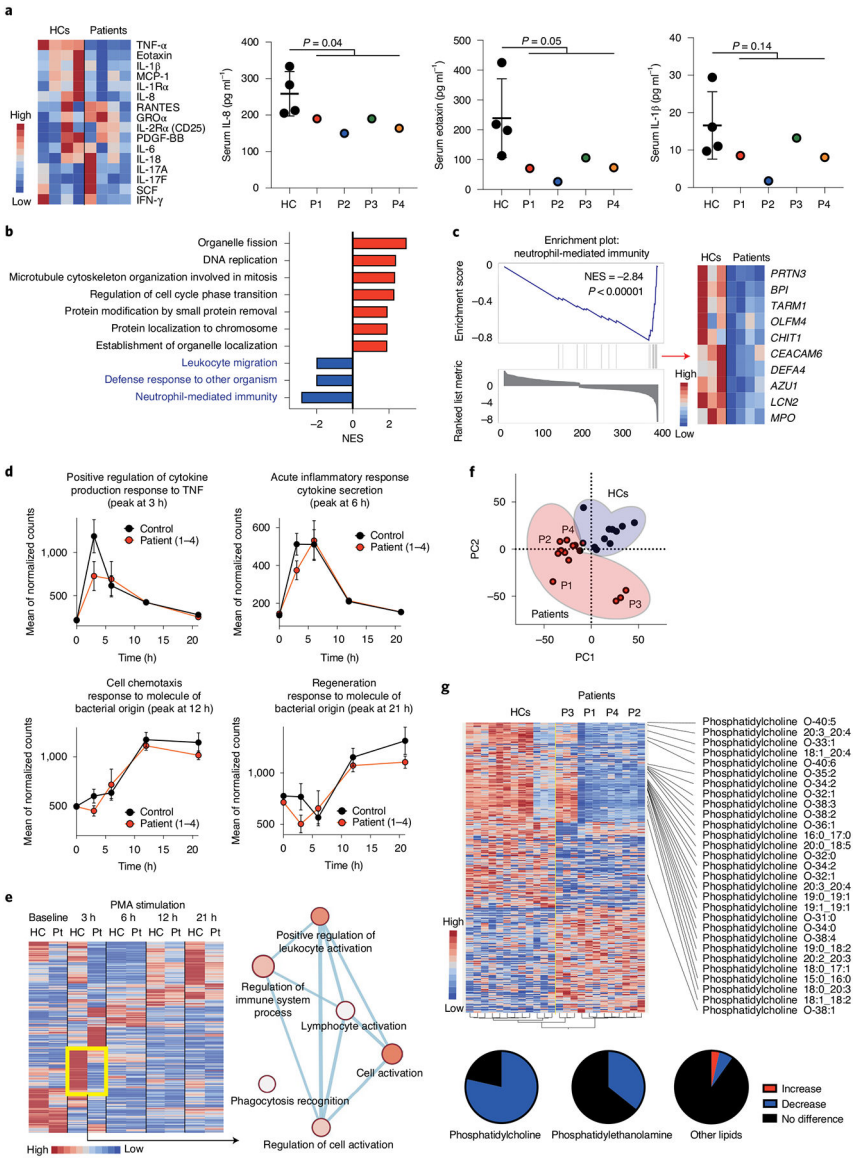

Fig. 3 |. Multi-omics analyses reveal iRHOM2 function in humans.

a, Results of cytokine array. The results are shown by heat map based on the ratio between patients and HCs (left panel). Actual data of IL-8, eotaxin-1 and IL-1β are shown (right panel, $n = 4$ for each HC and patient group). Data are mean ± s.d. and were analyzed by two-tailed, unpaired Student's *t*-test. **b**, GSEA of the patient whole-blood RNA-seq data in comparison with HCs after redundancy reduction. GSEA of differentially expressed genes in HCs versus patients. **c**, Results for the 'neutrophil-mediated immunity' gene set in GSEA. Enrichment plot and heat map for individual genes in the gene set are shown. NES, normalized enrichment score. **d**, Mean normalized counts comparing averages of patient and HC T cells for each highlighted gene set in Extended Data Fig. 3g ($n = 4$ per group). Error calculated is s.e.m. **e**, Heat map indicating the time course of gene expression for genes with significant differences between four HCs and four patients at 3 h of stimulation. Gene expression is shown as normalized counts of mRNA plotted along a scale, where blue

indicates low counts and red indicates high counts. Enrichment map of biological processes in the yellow square with connections between nodes signifying at least 65% overlap among the genes assigned to each node. **f**, Scatter plot of principal component axis one (PC1) and axis two (PC2) based on lipidomics data. Individual data points are colored according to patients and HCs and shading shows clusters. **g**, Cluster analysis of lipidomics data. Three technical repeats results are shown by heat map (left). Each specific lipid level of patients in comparison with the HCs is shown (right). Fractions of identified lipid species increased, decreased or no change (bottom). Statistical significance of the enrichment score was calculated by using an empirical phenotype-based permutation test (**b**,**c**). Pt, patient.

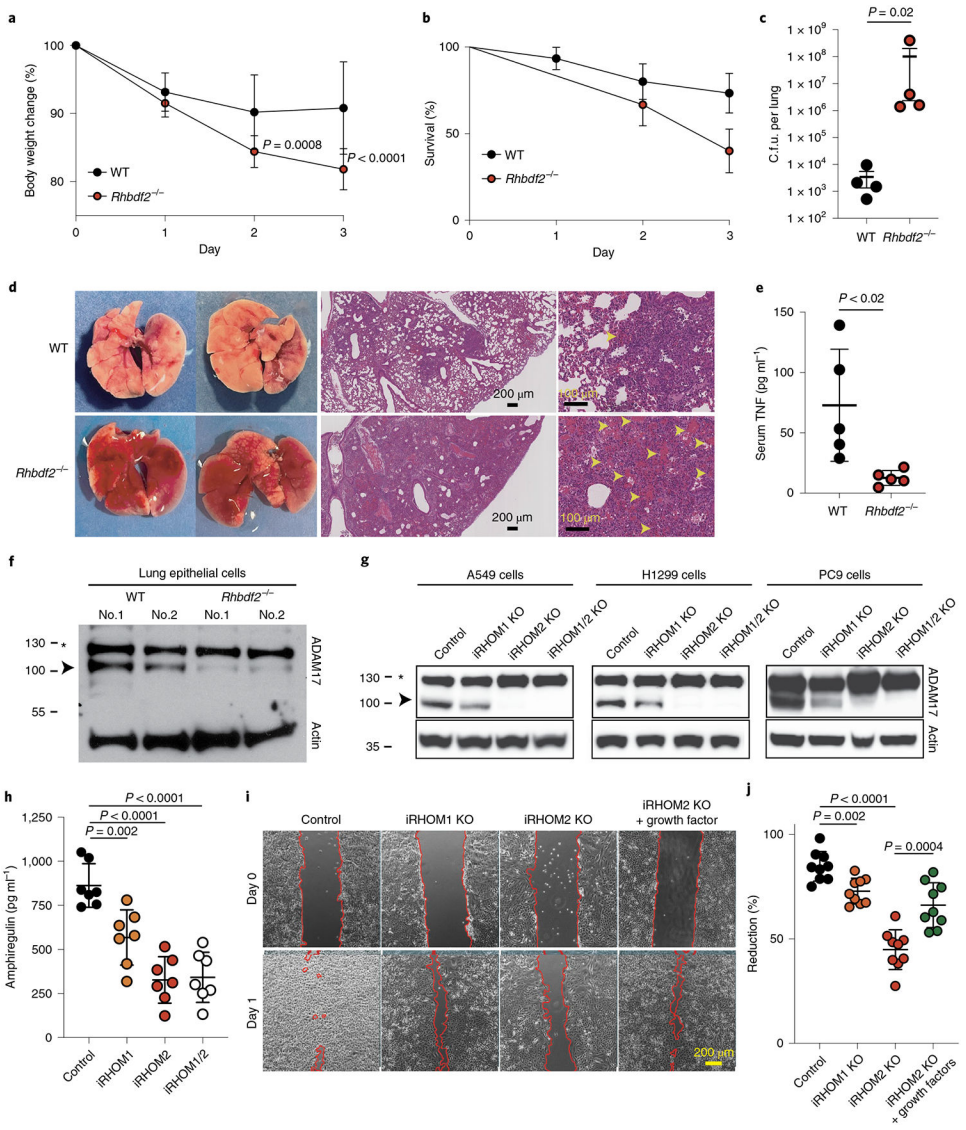

Fig. 4 |. iRHOM2 deficiency affects *P. aeruginosa* pneumonia and ADAM17 maturation and AREG secretion and function in lung epithelial cells.

a, Average of the change in body weight measurements for WT and *Rhbdf2*$^{-/-}$ mice infected with *P. aeruginosa* pneumonia during infection (n = 15 per group). **b**, Percentage of WT and *Rhbdf2*$^{-/-}$ mice who survived *P. aeruginosa* pneumonia averaged for total number of mice in each group over multiple trials of infection (n = 15 per group). Data are proportion ± s.e.m. **c**, Quantified c.f.u. of *P. aeruginosa* bacteria extracted from total lung tissue for each mouse (n = 4 per group). **d**, Lungs from *Rhbdf2*$^{-/-}$ mice infected with 5 × 10^8 c.f.u. of *P. aeruginosa* on day 3 following infection. Whole lung (left), lower magnification (middle) and higher magnification (right) are shown. Pulmonary hemorrhages are seen (yellow arrow). **e**, Bead-based multiplex assay measurements of TNF in mouse serum (n = 5 per group). **f**, Immunoblot of lung epithelial cells purified from two different WT or *Rhbdf2*$^{-/-}$ (knockout (KO)) mice. Asterisk shows pro-ADAM17, and black arrowhead shows mature ADAM17. **g**, Immunoblot as in **f**, of A549, H1299 and PC9 lung tumor cells knocked out

for the indicated targets. **h**, AREG measured by ELISA in cell culture supernatants of A549 cells treated with siRNAs as in Extended Data Fig. 4b ($n = 7$ per group). **i**, Wound healing assay in knockout A549 cells either with or without 50 ng ml^{-1} each of AREG, TGF-α and HB-EGF as growth factors. Scratches were made and repair of the scratch was evaluated 24 h later. **j**, Quantification of wound healing measured in **i** ($n = 9$ per group). Representative results of two (**f**) or three (**d**,**g**) independent experiments. Two-tailed, unpaired Student's *t*-test (**a**,**e**,**h**,**j**; mean ± s.d.) or Mann–Whitney test (**c**; mean ± s.e.m.) was used to calculate *P* value.

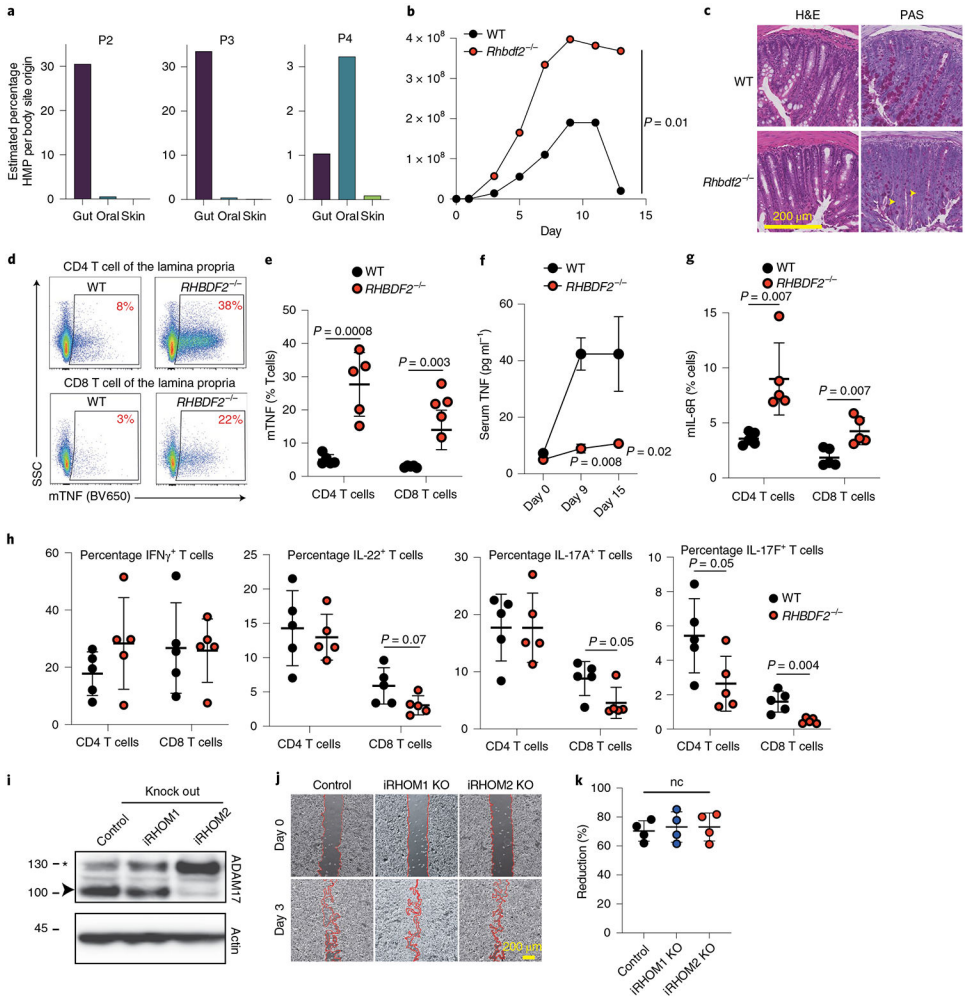

Fig. 5 |. iRHOM2 deficiency affects *C. rodentium* colitis and secretion of necessary cytokines in colon epithelial cells.

a, SourceTracker-based analysis of genera present in P2–4 stool. Likelihood of being sourced from gut, oral and skin microbiomes based on HMP data. **b**, Median c.f.u. per gram of stool for WT and *Rhbdf2*$^{-/-}$ mice versus days of infection. **c**, Hematoxylin and eosin (H&E) stain and periodic acid–Schiff (PAS) stain of colon samples for WT and *Rhbdf2*$^{-/-}$ mice at day 14 of *C. rodentium* infection. **d**, Flow cytometry dot plots quantitating surface mTNF expression on mice CD4 and CD8 T cells from lamina propria. **e**, Quantification of mTNF measured in **d**. **f**, Bead-based multiplex assay measurements of TNF in mouse serum during infection. **g**, Quantification of IL-6R measured in **f**. **h**, Percentage of CD4 and CD8 T cells in the lamina propia of WT and *Rhbdf2*$^{-/-}$ mice expressing IFN-γ, IL-22, IL-17A and IL-17F following infectious colitis as quantified by flow cytometry (gating strategy is shown in Extended Data Fig. 6). **i**, Immunoblot of SW620 colon tumor epithelial cells with either iRHOM1 or iRHOM2 knockout. Asterisk, pro-ADAM17; black arrowhead, mature ADAM17. β-actin as endogenous control. **j**, Wound healing assay in iRHOM KO SW620 cells. Scratches were made and evaluated 72 h later. **k**, Quantification of wound healing measured in **j** (n = 4 per group). C.f.u. data were from three independent experiments, with five mice in each WT or KO group per experiment. For pathological findings, serum TNF

and the cell phenotype of lamina propria were obtained from one (n = 10, respectively) out of three experiments. Two-way analysis of variance (**b**) or two-tailed, unpaired Student's t-test (**e**,**h**,**j**; mean ± s.d.) or Mann–Whitney test (**f**; mean ± s.e.m.). Representative result of three (**i**) or five (**c**) independent experiments. nc, no change.

Table 1 |

Patient characteristics

	Patient 1	Patient 2	Patient 3	Patient 4
Mutation	c.1887_1888delCT	c.2170_2171delCA	c.2170_2171delCA	c.2170_2171delCA
	p.Cys630LeufsTer19	p.Gln724ValfsTer105	p.Gln724ValfsTer105	p.Gln724ValfsTer105
Zygosity	Homozygous	Homozygous	Homozygous	Homozygous
Age, sex	8, M	8, M	4, F	1, M
Recurrent infections	Sinopulmonary otitis media	Upper respiratory tract	Upper respiratory tract	Sepsis colitis
Skin rash	Eczema at onset	No	No	Eczema at onset
Lymphadenopathy	No	No	No	No
Hepatosplenomegaly	Mild	No	No	Mild at presentation
Autoantibodies	Negative	N/A	N/A	Negative
HIES score	27	N/A	N/A	N/A
Thorax CT	Pneumatoceles bilateral infiltrates	Normal	Normal	Normal
PPD and TB culture	Negative	N/A	N/A	N/A
DHR test	Normal	Normal	Normal	Normal
Neutrophils (no. per μl) (1,400–6,200)	2,500	3,600	2,100	3,700
Monocytes (no. per μl) (0–700)	400	900	400	900
Eosinophils (no. per μl) (0–700)	140	710	290	360
Lymphocytes (no. per μl) (1,200–3,100)	2,100	3,400	4,100	7,700
Hgb (gl^{-1}) (12–17)	11.7	11.3	12.2	10.1
Plt (10^4 per μl)	233	385	408	458
$CD3^+$ T cells	70 (55–88)	74 (55–86)	69 (57–82)	61 (51–82)
$CD4^+$ T cells	34 (24–51)	38 (24–51)	46 (25–55)	31 (32–60)
Naive ($CD45RA^+$)	61 (42–82)	42 (42–82)	50 (55–85)	69 (52–97)
Memory ($CD45RO^+$)	39 (27–59)	57 (27–59)	50 (15–46)	28 (8–37)
$CD8^+$ T cells	33 (17–43)	31 (17–42)	21 (14–38)	31 (12–30)
Naive ($CD45RA^+$)	63 (40–94)	69 (40–94)	59 (46–100)	74 (48–111)
Memory ($CD45RA^-$)	35 (11–78)	30 (11–78)	39 (10–45)	24 (5–58)

	Patient 1	Patient 2	Patient 3	Patient 4
$CD19^+$ B cells	17 (7–23)	10 (7–23)	12 (10–31)	32 (11–40)
Naive (IgD^+CD27^-)	68 (6–91)	70 (6–91)	62 (54–94)	90 (80–98)
Memory (IgD^-CD27^+)	14 (7–31)	9 (7–31)	17 (3–32)	2 (1–9)
$CD16^-CD56^+$ NK cells	16 (4–29)	13 (4–29)	12 (3–29)	3.6 (2–28)
IgG	1031–1,180 (454–1,360)	656 (764–2,134)	936 (745–1,804)	200–683 (463–1,006)
IgM	87–111 (38–251)	72 (69–387)	155 (78–261)	129–111 (46–159)
IgA	200–245 (34–305)	164 (78–383)	203 (57–282)	<0.06 (17–69)
IgE	622–3156 (2–307)	80 (0–215)	50 (0–215)	9 (2–34)

Numeric patient data show range at 2 and 6 yr old. Age-matched references are in parentheses. M, male; F, female; N/A, not applicable; CT, computed tomography; PPD, purified protein derivative; TB, tuberculosis; DHR, dihydrorhodamine; Hgb, hemoglobin; Plt, platelets.